

1 **Supercooled liquid water clouds observed over Dome C,**
2 **Antarctica: temperature sensitivity and cloud radiative forcing**

3
4 **Philippe Ricaud¹, Massimo Del Guasta², Angelo Lupi³, Romain Roehrig¹, Eric Bazile¹,**
5 **Pierre Durand⁴, Jean-Luc Attié⁴, Alessia Nicosia³ and Paolo Grigioni⁵**

6
7 ¹CNRM, Université de Toulouse, Météo-France, CNRS, Toulouse, France

8 (philippe.ricaud@meteo.fr; romain.roehrig@meteo.fr; eric.bazile@meteo.fr)

9 ²INO-CNR, Sesto Fiorentino, Italy (massimo.delguasta@ino.cnr.it)

10 ³ISAC-CNR, Bologna, Italy (a.lupi@isac.cnr.it; a.nicosia@isac.cnr.it)

11 ⁴Laboratoire d'Aérogologie, Université de Toulouse, CNRS, UPS, Toulouse, France

12 (pierre.durand@aero.obs-mip.fr; jean-luc.attie@aero.obs-mip.fr)

13 ⁵ENEA, Roma, Italy (paolo.grigioni@enea.it)

14
15 Correspondence: philippe.ricaud@meteo.fr

16
17
18 ~~21-27~~ November 2023, Version REV03 ~~V01~~V02

19
20 Submitted to **Atmospheric Chemistry and Physics**

21

22

23 **Abstract**

24 Clouds affect the Earth climate with an impact that depends on the cloud nature (solid/
25 liquid water). Although the Antarctic climate is changing rapidly, cloud observations are sparse
26 over Antarctica due to few ground stations and satellite observations. The Concordia station is
27 located on the East Antarctic Plateau (75°S, 123°E, 3233 m above mean sea level), one of the
28 driest and coldest places on Earth. We used observations of clouds, temperature, liquid water
29 and surface irradiance performed at Concordia during 4 austral summers (December 2018-
30 2021) to analyse the link between liquid water and temperature and its impact on surface
31 irradiance in the presence of supercooled liquid water (liquid water for temperature less than
32 0°C) clouds (SLWCs). Our analysis shows that, within SLWCs, temperature logarithmically
33 increases from -36.0°C to -16.0°C when liquid water path increases from 1.0 to 14.0 g m⁻². The
34 SLWC ~~net~~-radiative forcing is positive and logarithmically increases from 0.0 to 70.0 W m⁻²
35 when liquid water path increases from 1.2 to 3.5 g m⁻². This is mainly due to the downward
36 longwave ~~downward~~ component that logarithmically increases from 0 to 90 W m⁻² when liquid
37 water path increases from 1.0 to 3.5 g m⁻². The attenuation of ~~solar-shortwave~~ incoming
38 irradiance (that can reach more than 100 W m⁻²) is almost compensated for by the upward
39 shortwave irradiance because of high values of surface albedo. Based on our study, we can
40 extrapolate that, over the Antarctic continent, SLWCs have a maximum ~~net~~-radiative forcing
41 rather weak over the Eastern Antarctic Plateau (0- to 7 W m⁻²) but 3 to 5 times larger over
42 Western Antarctica (0- to 40 W m⁻²), maximizing in summer and over the Antarctic Peninsula.

43

44 **1. Introduction**

45 Antarctic clouds play an important role in the climate system by influencing the Earth's
46 radiation balance, both directly at high southern latitudes and, indirectly, at the global level
47 through complex teleconnections (Lubin et al., 1998). However, in Antarctica, ground stations
48 are mainly located on the coast and yearlong observations of clouds and associated
49 meteorological parameters are scarce. Meteorological analyses and satellite observations of
50 clouds can nevertheless give some information on cloud properties suggesting that clouds vary
51 geographically, with a fractional cloud cover ranging from about 50 to 60% around the South
52 Pole to 80-90% near the coast (Bromwich et al., 2012; Listowski et al., 2019). In situ aircraft
53 measurements performed mainly over the Western Antarctic Peninsula (Grosvenor et al., 2012;
54 Lachlan-Cope et al., 2016) and nearby coastal areas (O'Shea et al., 2017) provided new insights
55 to polar cloud modelling and highlighted sea-ice production of Cloud-Condensation Nuclei
56 (CCN) and Ice Nucleating Particles (INPs) (see e.g. Legrand et al., 2016). Mixed-phase clouds
57 (made of solid and liquid water) are preferably observed near the coast (Listowski et al., 2019)
58 with larger ice crystals and water droplets (Lachlan-Cope, 2010; Lachlan-Cope et al., 2016;
59 Grosvenor et al., 2012; O'Shea et al., 2017; Grazioli et al., 2017). Based on the raDAR/liDAR-
60 MASK (DARDAR) spaceborne products (Listowski et al., 2019), it has been found that clouds
61 are mainly constituted of ice above the continent. The abundance of Supercooled Liquid Water
62 (SLW, the water staying in liquid phase below 0°C) clouds depends on temperature and
63 liquid/ice fraction. It decreases sharply poleward, and is two to three times lower over the
64 Eastern Antarctic Plateau than over the Western Antarctic. Furthermore, the nature and optical
65 properties of the clouds depend on the type and concentration of CCN and INPs. Bromwich et
66 al. (2012) mention in their review paper that CCN and INPs are of various nature and large
67 uncertainties exist relative to their origin and abundance over Antarctica. An important point
68 remains the inability of both research and operational weather prediction models to accurately

69 represent the clouds (especially SLW clouds, SLWCs) in Antarctica causing biases of several
70 tens $W m^{-2}$ on net surface irradiance (Listowski and Lachlan-Cope, 2017; King et al., 2006,
71 2015; Bromwich et al., 2013) over and beyond the Antarctic (Lawson and Gettelman, 2014;
72 Young et al. 2019). From year-long LIDAR observations of mixed-phase clouds at South Pole
73 (Lawson and Gettelman, 2014), SLWCs were shown to occur more frequently than in earlier
74 aircraft observations or weather model simulations, leading to biases in the surface radiation
75 budget estimates.

76 Liquid water in clouds may occur in supercooled form due to a relative lack of ice nuclei
77 for temperature greater than $-39^{\circ}C$ and less than $0^{\circ}C$. Very little SLW is then expected because
78 the ice crystals that form in this temperature range will grow at the expense of liquid droplets
79 (called the “Wegener-Bergeron-Findeisen” process; Wegener, 1911; Bergeron, 1928;
80 Findeisen, 1938; Storelvmo and Tan, 2015). Nevertheless, SLW is often observed at negative
81 temperatures higher than $-20^{\circ}C$ at all latitudes being a danger to aircraft since icing on the wings
82 and airframe can occur, reducing lift, and increasing drag and weight. As temperature decreases
83 to $-36^{\circ}C$, SLW dramatically lessens, so it is highly difficult 1) to observe SLWCs and 2) to
84 quantify the amount of liquid water present in SLWCs. But during the Year Of Polar Prediction
85 (YOPP) international campaign, recent observations performed at the Dome C station in
86 Antarctica of two case studies in December 2018 have revealed SLWCs with temperature
87 between $-20^{\circ}C$ and $-30^{\circ}C$ and Liquid Water Path (LWP, the liquid water content integrated
88 along the vertical) between 2 to $20 g m^{-2}$, as well as a considerable impact on the net surface
89 irradiance that exceeded the simulated values by 20- to 50 $W m^{-2}$ (Ricaud et al., 2020).

90 The Dome C (Concordia) station, jointly operated by French and Italian institutions in the
91 Eastern Antarctic Plateau ($75^{\circ}06'S$, $123^{\circ}21'E$, 3233 m above mean sea level, amsl), is one of
92 the driest and coldest places on Earth with surface temperatures ranging from about $-20^{\circ}C$ in
93 summer to $-70^{\circ}C$ in winter. There are four main instruments relevant to this study that have

94 been routinely running for about 10 years: 1) The H₂O Antarctica Microwave Stratospheric and
 95 Tropospheric Radiometer (HAMSTRAD, Ricaud et al., 2010a) to obtain vertical profiles of
 96 temperature and water vapour, as well as the LWP. 2) The tropospheric depolarization LIDAR
 97 (Tomasi et al., 2015) to obtain vertical profiles of backscatter and depolarization to be used for
 98 the detection of SLWCs. 3) An Automated Weather Station (AWS) to provide screen-level air
 99 temperature. And 4) the Baseline Surface Radiation Network (BSRN) station to measure
 100 ~~downward and upward surface~~ longwave (4- to 50 μm) and shortwave (0.3- to 3 μm),
 101 ~~downward and upward~~ surface irradiances (F) from which the net surface irradiance (F_{Net}),
 102 calculated as the difference between the downward and upward components, can be computed
 103 (Driemel et al., 2018) as:

$$F_{Net} = (F_{LW}^{Down} - F_{LW}^{Up}) + (F_{SW}^{Down} - F_{SW}^{Up}) \quad (1)$$

105 where F_{LW}^{Down} , F_{LW}^{Up} , F_{SW}^{Down} , and F_{SW}^{Up} represent the ~~downward~~ longwave ~~downward~~, ~~upward~~
 106 longwave ~~upward~~, ~~downward~~ shortwave ~~downward~~ and ~~upward~~ shortwave ~~upward~~ surface
 107 irradiances, respectively.

108 ~~At a given time, the impact of a cloud on the surface irradiance is estimated from the~~
 109 ~~difference between the net irradiance, in cloudy ($F_{Net,cloud}$) and cloud-free (FCF_{Net}) conditions~~
 110 ~~to provide the so-called~~ ~~At a given time, the impact of a cloud on the surface irradiance can be~~
 111 ~~estimated by subtracting what would have been the cloud-free surface irradiance from the~~
 112 ~~measured surface irradiance, to provide the so-called “cloud radiative forcing” ΔF_{Net} (e.g.,~~
 113 ~~Stapf et al., 2020):~~

$$\Delta F_{Net} = F_{Net,cloud} - FCF_{Net} \quad (2)$$

115 ~~A similar equation can be written for each of the four irradiances that appear in the right-hand-~~
 116 ~~side of equation (1).~~ The aim of the present study is double. Using observations performed at
 117 Concordia, we intend to quantify the link between 1) temperature in the SLWCs and LWP and
 118 2) SLWC radiative forcing and LWP.

- Mis en forme : Couleur de police : Automatique
- Mis en forme : Couleur de police : Automatique
- Mis en forme : Couleur de police : Automatique
- Mis en forme : Couleur de police : Automatique
- Mis en forme : Couleur de police : Automatique
- Mis en forme : Couleur de police : Automatique
- Mis en forme : Centré, Retrait : Première ligne : 0 cm, Taquets de tabulation : 6,75 cm, Centré + 16 cm, Droite
- Mis en forme : Couleur de police : Automatique
- Mis en forme : Couleur de police : Automatique
- Mis en forme : Couleur de police : Automatique
- Mis en forme : Couleur de police : Automatique
- Mis en forme : Couleur de police : Automatique
- Mis en forme : Couleur de police : Automatique
- Mis en forme : Couleur de police : Automatique
- Mis en forme : Retrait : Première ligne : 0 cm

119

120 The article is structured as follows. Section 2 presents the instruments during the period of
121 study. In section 3, we detail the methodology employed to detect the SLWCs and calculate
122 their cloud radiative forcing, and we present the statistical method to emphasize the relationship
123 between in-cloud temperature and LWP on the one hand, and cloud radiative forcing and LWP
124 on the other hand. The results are highlighted in section 4 and discussed in section 5, before
125 concluding in section 6.

126

127 **2. Instruments**

128 We have used the observations from 4 instruments held at the Dome C station, namely the
129 LIDAR instrument to classify the cloud as SLWC, the HAMSTRAD microwave radiometer to
130 obtain LWP and vertical profile of temperature, the AWS to obtain screen-level air temperature
131 and the BSRN network to measure the surface irradiances (F_{LW}^{Down} , F_{LW}^{Up} , F_{SW}^{Down} , and F_{SW}^{Up}) to
132 obtain F_{Net} .

133 *2.1. LIDAR*

134 The tropospheric depolarization LIDAR (532 nm) has been operating at Dome C since 2008
135 (see http://lidarmax.altervista.org/englidar/_Antarctic%20LIDAR.php). The LIDAR provides
136 5-min tropospheric profiles of clouds characteristics continuously, from 20 to 7000 m above
137 ground level (agl), with a resolution of 7.5 m. For the present study, the most relevant parameter
138 is the LIDAR depolarization ratio (Mishchenko et al., 2000) that is a robust indicator of non-
139 spherical shape for randomly oriented cloud particles. A depolarization ratio below 10% is
140 characteristic of SLWC, while higher values are produced by ice particles. The possible
141 ambiguity between SLW droplets and oriented ice plates is avoided at Dome C by operating
142 the LIDAR 4° off-zenith (Hogan and Illingworth, 2003).

143 *2.2. HAMSTRAD*

144 HAMSTRAD is a microwave radiometer that profiles water vapour, liquid water and
145 tropospheric temperature above Dome C. Measuring at both 60 GHz (oxygen molecule line
146 (O₂) to deduce the temperature) and 183 GHz (H₂O line), this unique, state-of-the-art
147 radiometer was installed on site for the first time in January 2009 (Ricaud et al., 2010a and b).
148 The measurements of the HAMSTRAD radiometer allow the retrieval of the vertical profiles
149 of water vapour and temperature from the ground to 10-km altitude with vertical resolutions of
150 30 to 50 m in the Planetary Boundary Layer (PBL), 100 m in the lower free troposphere and
151 500 m in the upper troposphere-lower stratosphere. The integral along the vertical of the water
152 vapour concentration gives the integrated water vapour (IWV). The time resolution is adjustable
153 and fixed at 60 seconds since 2018. Note that an automated internal calibration is performed
154 every 12 atmospheric observations and lasts about 4 minutes. Consequently, the atmospheric
155 time sampling is 60 seconds for a sequence of 12 profiles and a new sequence starts 4 minutes
156 after the end of the previous one. The temporal resolution on the instrument allows for detection
157 and analysis of atmospheric processes such as the diurnal evolution of the PBL (Ricaud et al.,
158 2012) and the presence of clouds and diamond dust (Ricaud et al., 2017) together with SLWCs
159 (Ricaud et al., 2020). In addition, the LWP (g m⁻²) that gives the amount of liquid water
160 integrated along the vertical can also be estimated. Observations of LWP have been performed
161 when the instrument was installed at the Pic du Midi station (2877 amsl, France) during the
162 calibration/validation period in 2008 prior to its set up in Antarctica in 2009 (Ricaud et al.,
163 2010a) and during the Year Of Polar Prediction (YOPP) campaign in summer 2018-2019
164 (Ricaud et al., 2020). At the present time, it has not yet been possible to compare HAMSTRAD
165 LWP retrievals with observations from other instruments, neither at the Pic du Midi nor at
166 Dome C stations. To better evaluate its performance, the 2021-2022 and the future 2022-2023
167 summer campaigns are dedicated to in-situ observations of SLWCs. Comparisons with
168 numerical weather prediction models were showing consistent amounts of LWP at Dome C

169 when the partition function between ice and liquid water was favouring SLW for temperatures
170 less than 0°C (Ricaud et al., 2020). Note that microwave observations at 60 and 183 GHz are
171 not sensitive to ice crystals. This has already been discussed in Ricaud et al. (2017) when
172 considering the study of diamond dust in Antarctica. As a consequence, possible precipitation
173 of ice, within or below SLW clouds, as detected by the LIDAR, does not affect the retrievals of
174 temperature, water vapour and liquid water.

175 2.3. AWS

176 An American Automated Weather Station (AWS) is installed at Concordia about 500 m
177 away from the station and can provide screen-level air temperature (T_a) every 10 minutes. Data
178 are freely available at <https://amrc.ssec.wisc.edu/data/archiveaws.html>.

179 2.4. BSRN

180 The BSRN sensors at Dome C are mounted at the Astroconcordia/Albedo-Rack sites, with
181 upward and downward looking, heated and ventilated Kipp&Zonen CM22 pyranometers and
182 CG4 pyrgeometers providing measurements of hemispheric downward and upward broadband
183 shortwave (SW, 0.3– to 3 μm) and longwave (LW, 4– to 50 μm) horizontal irradiances at the
184 surface, respectively. These data are used to retrieve values of net surface irradiances. All these
185 measurements follow the rules of acquisition, quality check and quality control of the BSRN
186 (Driemel et al., 2018).

187 2.5. Period of study

188 From the climatological study presented in Ricaud et al. (2020), the SLWCs are mainly
189 observed above Dome C in summer, with a higher occurrence in December than in January:
190 26% in December against 19% in January representing the percentage of days per month that
191 SLW clouds were detected during the YOPP campaign (summer 2018-2019) within the LIDAR
192 data for more than 12 hours per day. We have thus concentrated our analysis on December and
193 the 4 years: 2018-2021. Since we have to use the four data sets (LIDAR, HAMSTRAD, AWS

194 and BSRN) in time coincidence, the actual number of days per year and the time sampling for
195 each day selected in our analysis are detailed in Table 1.

196

197 **3. Methodology**

198 *3.1. SLWC detection*

199 Consistent with Ricaud et al. (2020), we use LIDAR observations to discriminate between
200 SLW and ice in a cloud. High values of LIDAR backscatter coefficient ($\beta > 100 \beta_{\text{mol}}$, with β_{mol}
201 the molecular backscatter) associated with very low depolarization ratio (<5%) signifies the
202 presence of an SLWC whilst high depolarization ratio (>20%) indicates the presence of an ice
203 cloud or precipitation. Once the SLWC is detected both in time and altitude, the temperature
204 (T) profile within the cloud and the LWP measured by the HAMSTRAD radiometer in time
205 coincidence are selected together with the surface irradiances observed by the BSRN
206 instruments.

207 The LIDAR profiles are interpolated along the temperature vertical grid and then according
208 to the temperature time sampling. As a consequence, for a given time and height, we have a
209 depolarization ratio, a backscatter value, a ~~regular~~ temperature as well as ~~a~~ (not height-
210 dependent) IWV and LWP values. ~~The same method is used for F_s .~~ BSRN irradiances F_s are
211 time interpolated to be coincident with the other parameters. So, for a given time, we have a set
212 of BSRN irradiances F_s (F_{LW}^{Down} , F_{LW}^{Up} , F_{SW}^{Down} , F_{SW}^{Up} and F_{Net}) and an LWP. At a (time, height)
213 point showing high backscatter signal and low depolarization, the associated parameters
214 (temperature, LWP and irradiances F_s) are flagged as “SLW cloud”. The statistic is thus done
215 using all the SLW-flagged points without any averaging. The temperature corresponds to the
216 in-cloud temperature.

217 Figure 1 shows, as a typical example, the time evolution of the LIDAR backscatter
218 coefficient and depolarization ratio, as well as the HAMSTRAD LWP and temperature vertical

219 profile for the 27 December 2021. Associated with the SLWCs, the LWP values are between
220 1.0 and -3.0 g m⁻². The SLWCs are present over a temperature range varying from about -28.0
221 °C to -33.0 °C. Note the cloud present at 04:00-05:00 UTC that is not labelled as a SLWC but
222 rather as an ice cloud (high backscatter and high depolarization signals) with no associated
223 increase of LWP and temperature above -28.0 °C.

224 Figure 2 highlights the time evolution of the SLWC obtained on 27 December 2021
225 together with some snapshots from the HALO-CAM video camera taken with or without SLWC
226 on: 01:00 (no SLWC), 07:19 (SLWC), 09:00 (no SLWC), 10:14 (SLWC), 13:00 (no SLWC),
227 16:03 (SLWC), 18:01 (no SLWC) and 20:53 UTC (SLWC). SLWCs (high backscatter and low
228 depolarization signals) are clearly detected at 07:00-08:00, 10:00-11:00, 16:00-17:00, 21:00-
229 22:00 and 23:00-24:00 UTC over an altitude range 500-to 1000 m above ground level (agl). In
230 general, SLWCs observed over the station did not correspond to overcast conditions.

231 3.2. Cloud Radiative Forcing

232 ~~The cloud radiative forcing (ΔF) can be defined as:~~
233 ~~$$\Delta F = F - F_{CF} \quad (2)$$~~
234 ~~for the net, longwave downward, longwave upward, shortwave downward and shortwave~~
235 ~~upward surface irradiances, with F_{CF} being the surface irradiance in cloud free conditions.~~
236 ~~From equation (2), ~~One one~~ of the main difficulties in computing the cloud radiative forcing~~
237 ~~(ΔF_{Net})- ΔF is to estimate $F_{CF_{Net}}$ - F_{CF} from its individual components, namely the cloud-free~~
238 ~~downward longwave, upward longwave, downward shortwave and upward shortwave surface~~
239 ~~irradiances. We performed ~~Several several~~ studies ~~have been performed~~ (reference irradiances~~
240 ~~measured over ~~one~~ days when clouds are absent, radiative transfer calculations) ~~but from which~~~~
241 ~~it resulted that~~ the most robust method ~~has been was~~ to use a parameterization of the ~~cloud-free~~
242 downward longwave and shortwave surface irradiances widely used in the community. In

243 Dutton et al. (2004), cloud-free downward shortwave surface irradiance (FCF_{SW}^{Down}) is
244 parameterized as:

$$245 \quad FCF_{SW}^{Down} = a \cos(z)^b c^{\left(\frac{1}{\cos(z)}\right)} \quad (3)$$

246 where z is the solar-zenith angle, and a , b , and c are coefficients optimized using well-identified
247 cloud-free situations. In Dupont et al. (2008), cloud-free downward longwave surface
248 irradiance (FCF_{LW}^{Down}) is parameterized as:

$$249 \quad FCF_{LW}^{Down} = \varepsilon_a \sigma T_a^4 \quad (4)$$

250 where T_a is the screen-level air temperature in Kelvin (K), σ the Stephan-Boltzmann's constant
251 and ε_a the apparent atmospheric emissivity. The latter is supposed to be a function of the
252 integrated water vapor (IWV) following the equation:

$$253 \quad \varepsilon_a = 1 - (1 + IWV) \exp(-(d + e \times IWV)^f) \quad (5)$$

254 where d , e and f are coefficients that need to be optimized using cloud-free situations and IWV
255 is provided by the HAMSTRAD measurements. The cloud-free upward shortwave surface
256 irradiance (FCF_{SW}^{Up}) is evaluated from FCF_{SW}^{Down} with the surface albedo ($A_{BSRN} =$
257 $F_{SW}^{Up}(BSRN)/F_{SW}^{Down}(BSRN)$) calculated from observations:

$$258 \quad FCF_{SW}^{Up} = A_{BSRN} \times FCF_{SW}^{Down} \quad (6)$$

259 where $F_{SW}^{Up}(BSRN)$ and $F_{SW}^{Down}(BSRN)$ are the upward and downward shortwave surface
260 irradiance measured by the BSRN instruments, respectively. With this method, we take into
261 account the actual shape of the surface, and in particular its rough structure caused by the
262 sastrugi (see section 5.5). Thus, the surface albedo varies with the sun angles (azimutal and
263 zenithal) and cannot be considered as constant over the diurnal cycle. ~~Note that computationally
264 simple, theoretically based parameterization for the broadband albedo of snow and ice can
265 accurately reproduce the theoretical broadband albedo under a wide range of snow, ice, and
266 atmospheric conditions (Gardner and Sharp, 2010).~~

267 The cloud-free upward longwave radiation (FCF_{LW}^{Up}) is evaluated as:

$$268 \quad FCF_{LW}^{Up} = \varepsilon_s \sigma T_s^4 + (1 - \varepsilon_s) FCF_{LW}^{Down} \quad (7)$$

269 where T_s is the surface temperature and the surface emissivity ε_s is assumed constant and equal
270 to 0.99. ~~Screen-level temperatures T_a are provided by the American automated weather station~~
271 ~~(AWS) situated at 500 m from the Concordia base.~~ T_s is diagnosed based on equation (7) by
272 using the BRSN upward and downward longwave surface irradiances. ~~IWV is provided by the~~
273 ~~HAMSTRAD measurements.~~

274 Cloud-free situations are detected based on visual inspection of the LIDAR
275 (depolarization) measurements. Depolarization ratios greater than about 1% are attributed to
276 the presence of cloud (cirrus, mixed-phase, SLW), diamond dust, fog, etc. Thus, within each
277 24-hour slot covering the Decembers 2018-2021, the 1-hour periods when the depolarization
278 ratios are less than 1% are considered as cloud-free periods. Consequently, to evaluate the
279 surface cloud-free irradiances over the month of December and the years 2018-2021, we need
280 to have coincident observations from the 4 BSRN instruments, the LIDAR (depolarization),
281 HAMSTRAD and the AWS (see Table 1).

282 Once cloud-free situations are identified, the parametric coefficients $a-f$ are estimated
283 minimizing a least-square cost function using the trust region reflective method (e.g., Branch
284 et al., 1999). To assess the robustness of the estimated coefficient values, a K-fold cross-
285 validation is performed. The learning dataset is split into 10 subsamples of equal size. ~~9-Nine~~
286 of them are selected to optimize the coefficient and the validation is conducted on the remaining
287 subsample. The exercise is performed 10 times. The results are summarized below. Note that
288 following Dupont et al. (2008), f is assumed to be equal to 1.0, and therefore not optimized.

289 For cloud-free downward shortwave surface irradiance, the K-fold cross-validation
290 provides the following K-fold average value (K-fold minimum and maximum are indicated
291 within brackets): $a = 1360.7 [1360.5, 1360.8] \text{ W m}^{-2}$; $b = 0.990 [0.989, 0.991]$; $c = 0.964 [0.964,$

292 0.965] giving a bias of -0.002 [-0.317, 0.251] W m⁻² and a RMSE of 14.9 [10.8, 16.5] W m⁻².
293 Similarly, for cloud-free downward longwave surface irradiance, the K-fold cross-validation
294 provides the following results: d = 0.723 [0.722, 0.724]; e = 3.58 [3.57, 3.59] kg⁻¹ m²; f = 1.0
295 giving a bias of 0.34 [-0.005, 0.87] W m⁻² and a RMSE of 9.26 [8.92, 9.58] W m⁻². These
296 coefficient values are then used to compute cloud-free surface irradiances at a 1-min time
297 resolution.

298 Figure 3 shows the time evolution of the cloud radiative forcing (ΔF_{net}) and the individual
299 components (ΔF_{LW}^{Down} , ΔF_{LW}^{Up} , ΔF_{SW}^{Down} and ΔF_{SW}^{Up}) calculated for 27 December 2021 when
300 SLWCs are present (see Figures 1 and 2). Associated with the SLWCs, on the one hand,
301 ΔF_{LW}^{Down} increases to values of +40- to 90 W m⁻², whilst the impact on ΔF_{LW}^{Up} is negligible (± 2
302 W m⁻²). On the other hand, ΔF_{SW}^{Down} and ΔF_{SW}^{Up} both similarly decrease by 80- to 150 W m⁻².
303 The effect on ΔF_{net} is obviously positive (0- to 80 W m⁻²) with some weak negative values
304 (from 0 to -10 W m⁻²) when SWLCs just appear or disappear and that can possibly come from
305 the inhomogeneity of the cloud distribution. Spikes can be attributed to cloud edge effects,
306 when a fraction of the direct fraction of the shortwave solar incident radiation and an additional
307 diffuse contribution scattered from cloud edges falls on the radiation sensor.

308 We now want to statistically analyse all the ΔF calculated in December 2018-2021 in order
309 to assess the SLWC radiative forcing as a function of LWP and to investigate the sensitivity of
310 the temperature inside the SLWCs as a function of LWP.

311 3.3. Statistical Method

312 The datasets corresponding to SLWCs periods are binned into 1°C-wide bins for in-cloud
313 temperature T , 0.2 g m⁻²-wide bins for LWP, and 5 W m⁻²-wide bins for ΔF . The number of
314 points per bin is calculated for all the paired datasets, namely T -LWP, and ΔF -LWP (ΔF_{net} -
315 LWP, ΔF_{LW}^{Down} -LWP, ΔF_{LW}^{Up} -LWP, ΔF_{SW}^{Down} -LWP and ΔF_{SW}^{Up} -LWP). The 2D probability density

316 (PD) is calculated for the paired datasets and defined as $PD_{ij} = 100 \frac{N_{ij}}{N_t}$, where N_{ij} and N_t are
317 the count number in the bin ij and the total count number ($N_t = \sum_{j=1}^N \sum_{i=1}^M N_{ij}$), respectively,
318 with M and N being the total number of bins in LWP on one side, and in temperature or ΔF on
319 the other side, respectively. So, for each value of T_j (within a 1°C-wide bin j) or ΔF_j (within a
320 5 W m⁻²-wide bin j), a weighted average of LWP (\overline{LWP}_j) is calculated together with its
321 associated weighted standard deviation (σ_{LWP_j}), considering all the LWP_{ij} values (within 0.2 g
322 m⁻²-wide bins) from $i=1$ to M , with M the total number of LWP bins and w_{ij} the weight, namely
323 the number of points ($w_{ij} = N_{ij}$), associated to the bin ij :

$$324 \quad \overline{LWP}_j = \frac{\sum_{i=1}^M w_{ij} LWP_{ij}}{\sum_{i=1}^M w_{ij}} \quad (8)$$

325 and

$$326 \quad \sigma_{LWP_j} = \sqrt{\frac{\sum_{i=1}^M w_{ij} (LWP_{ij} - \overline{LWP}_j)^2}{\sum_{i=1}^M w_{ij}}} \quad (9)$$

327 For each T and ΔF dataset, the distribution of the total count numbers N_{tj} per 1°C or
328 5 W m⁻²-wide bin ($N_{tj} = \sum_{i=1}^M N_{ij}$ with $j = 1, \dots, N$) can be fitted by a function $N(x)$, with $x =$
329 T or ΔF , based on 2 to 3 Gaussian distributions as:

$$330 \quad N(x) = \sum_{k=1}^{2 \text{ or } 3} a_k \exp\left(-\frac{1}{2} \left(\frac{x - \mu_k}{\sigma_k}\right)^2\right) + c_0 \quad (10)$$

331 with a_k , μ_k and σ_k being the amplitude, the mean and the standard deviation of the k^{th} Gaussian
332 function and c_0 is a constant. We have used 0, 2 or 3 Gaussians for ΔF components and 3
333 Gaussians for T (“0” means that no Gaussian fit was meaningful). Table 2 lists all the fitted
334 parameters (a_k , μ_k , σ_k and c_0 with $k = 0$ to 3).

335 In the relationship between x (T or ΔF) and LWP, we have considered x_j (T_j or ΔF_j) to be
336 significant when:

$$337 \quad |x_j - \mu_k| \leq \sigma_k \text{ for } k = 1 - 2 \text{ or } 3 \text{ (for } \Delta F) \text{ or } 1 - 3 \text{ (for } T) \quad (11)$$

338 and used for this significant point its average value and standard deviation, \overline{LWP}_j and σ_{LWP_j} ,
339 respectively, with $j = 1, \dots, N$.

340 Finally, a logarithmic function of the form

$$341 \quad x = \alpha + \beta \ln(\overline{LWP}) \quad (12)$$

342 has been fitted onto these significant points where the retrieved constants α and β are shown in
343 Table 3 for x being T , ΔF_{net} , ΔF_{LW}^{Down} , ΔF_{LW}^{Up} , ΔF_{SW}^{Down} and ΔF_{SW}^{Up} .

344

345 4. Results

346 4.1. Temperature-Liquid Water Relationship in SLWCs

347 The relationship between temperature and LWP within SLWCs over the 4-summer period
348 at Dome C is presented Figure 4 left in the form of a Probability Density (PD) that is the fraction
349 of points within each bin of 0.2 g m^{-2} width in LWP and 1.0°C width in temperature. It clearly
350 shows a net tendency for liquid water to increase with temperature, up to $\sim 14 \text{ g m}^{-2}$ in LWP and
351 -18°C in temperature, with two zones having a density as high as $\sim 2\%$, at $[0.5 \text{ g m}^{-2}, -33^\circ\text{C}]$
352 and $[1.5 \text{ g m}^{-2}, -32^\circ\text{C}]$. We have performed a weighted average of the LWPs within each
353 temperature bin (Figure 4 centre). Then, we have fitted 3 Gaussian distributions to the count
354 numbers as a function of temperature (Figure 4 right). If we now only consider temperature
355 bins within one-sigma of the centre of the Gaussian distributions, we can fit the following
356 logarithmic relation of the temperature T as a function of LWP within the SLWC (Figure 4
357 centre):

$$358 \quad T(LWP) = -33.8 (\pm 1.5) + 6.5 \ln(LWP) \quad (13)$$

359 for $T \in [-36; -16]^\circ\text{C}$ and $LWP \in [1.0; 14.0] \text{ g m}^{-2}$, with a validity range where ($\pm 1.5^\circ\text{C}$)
360 corresponds to the range where the relationship is valid within indicated by the 2 blue dashed
361 lines ($\pm 1.5^\circ\text{C}$) in Figure 4 centre. In other words, based on our study, we have a clear evidence
362 that supercooled liquid water content exponentially increases with temperature. Considering

363 the temperature vs. LWP relationship, the two main Gaussian distributions are centered around
 364 -28°C and -30°C , corresponding to temperatures usually encountered in Concordia whilst the
 365 third one, far much less intense, is centered around -18°C , probably the signature of very
 366 unusual events occurring in Concordia as the warm-moist events. Episodes of warm-moist
 367 intrusions exist above Concordia originated from mid-latitudes (Ricaud et al., 2017 and 2020)
 368 and are known as “atmospheric rivers” (Wille et al., 2019). Although they are infrequent, they
 369 can provide high values of temperature and LWP.

370 4.2. Radiative Forcing-Liquid Water Relationship in SLWC conditions

371 Although the amount of LWP is very low ($\lll 20 \text{ g m}^{-2}$) at Dome C compared to what can
 372 be measured and modelled (Lemus et al., 1997) in the Arctic (50- to 75 g m^{-2}) and at
 373 middle/tropical latitudes (100- to 150 g m^{-2}), we intended to estimate its impact on the cloud
 374 radiative forcing at Dome C. In Figures 5 to 9, the left panel presents the PDs of the cloud
 375 radiative forcing ΔF_{net} ~~$-\Delta F$~~ as a function of the LWP, and for the individual components that
 376 contribute to the cloud radiative forcing: ~~for $-\Delta F_{net}$, $-\Delta F_{LW}^{Down}$, ΔF_{LW}^{Up} , ΔF_{SW}^{Down} and ΔF_{SW}^{Up} ,~~
 377 respectively. The central panel shows, for the same parameters, the corresponding weighted
 378 average LWP within 5 W m^{-2} -wide bins of ΔF whereas the right panel shows the corresponding
 379 count number within 5 W m^{-2} -wide bins fitted by 2 or 3 Gaussian distributions (or no Gaussian
 380 distribution when it becomes impossible).

381 Based on our analysis, the relationship between ΔF_{net} (W m^{-2}) and the LWP (g m^{-2}) has
 382 been estimated as:

$$383 \quad \Delta F_{net}(LWP) = -18.0 (\pm 10.0) + 70.0 \ln(LWP) \quad (14)$$

384 for $\Delta F_{net} \in [0; 70] \text{ W m}^{-2}$ and $LWP \in [1.2; 3.0] \text{ g m}^{-2}$, where with a validity range indicated
 385 ($\pm 10.0 \text{ W m}^{-2}$) corresponds to the range where the relationship is valid within the two blue
 386 dashed lines ($\pm 10.0 \text{ W m}^{-2}$) in Figure 5 centre. Thus, for LWP greater than 1.2 g m^{-2} , our study

387 clearly shows that the cloud radiative forcing induced by the presence of SLWCs above
388 Concordia is positive and can reach 70 W m^{-2} for an LWP of 3.0 g m^{-2} .

389 The splitting of the cloud radiative forcing between each of its four components can be
390 evaluated from their individual relationships with the LWP. These relations are gathered in
391 Table 3, established from the plots presented in Figures 5 to 9. They are of the same form as
392 for ~~net~~-cloud radiative forcing, i.e. a logarithmic dependence on LWP. Table 3 presents the
393 coefficients α and β of the logarithmic function $f(LWP) = \alpha + \beta \ln(LWP)$ for the temperature
394 T or the radiation components ΔF , together with the valid range of these relations for T , ΔF and
395 LWP. For the values presented in Table 3, our study clearly shows that SLWCs have a positive
396 impact on ΔF_{LW}^{Down} increasing from 0 to 90 W m^{-2} for LWP ranging from 1.0 to 3.5 g m^{-2} , a
397 negative impact on ΔF_{SW}^{Down} and ΔF_{SW}^{Up} decreasing from 0 to -130 and -110 W m^{-2} , respectively
398 for LWP ranging from 1.5 to 4.0 g m^{-2} , and negligible impact ($\pm 5 \text{ W m}^{-2}$) on ΔF_{LW}^{Up} for LWP
399 ranging from 0 to 6.5 g m^{-2} . Considering the absolute values of ΔF vs. LWP relationship
400 (keeping aside ΔF_{LW}^{Up}), we have systematically the most intense Gaussian distributions centered
401 at $\sim 10 \text{ W m}^{-2}$, and the other ones centered at $\sim 55 \text{ W m}^{-2}$ and $\sim 80 \text{ W m}^{-2}$.

402 To synthesize, our study showed that the major impact of SLWCs on net surface irradiance
403 is an increase of downward longwave component (~~0 to~~ -80 W m^{-2}), whereas it has a marginal
404 impact on upward longwave component since this parameter is mainly dependent on T_s which
405 results from various meteorological forcings. In the presence of SLWC, the attenuation of
406 ~~shortwavesolar~~ incoming irradiance (which can overpass 100 W m^{-2}) is almost compensated
407 for by the upward shortwave irradiance because of high values of surface albedo.

408 We can also estimate the sensitivity of the longwave component to temperature and
409 humidity by considering the values of the equivalent atmospheric emissivity ϵ_a used in the
410 equations 4-7. On the one side, the values of IWV observed at Dome C are very low even in
411 summer, typical summertime values are between 0.8 and 1.2 kg m^{-2} (Ricaud et al., 2020). This

412 corresponds to values of ε_a between 0.950 and 0.985, i.e. a relative variation of the order of
 413 3.6%. On the other side, a variation ΔT of the screen-level air (surface) temperature T_a (T_s) has
 414 a relative impact on the downwelling (upwelling) longwave irradiance of the order of $4 \Delta T/T_a$
 415 ($4 \Delta T/T_s$), which amounts to around 1.6% per degree of ΔT . Given that observations of surface
 416 and screen-level air temperatures reveal variations of several degrees, both in their diurnal cycle
 417 and from a day to another, we can conclude that the impact of temperature on longwave
 418 irradiance variations is larger than that of IWV.

419

420 5. Discussion

421 5.1 Relation with critical temperature

422 Our study shows that, above Concordia, there is an exponential dependence of LWP on both
 423 temperature and cloud radiative forcing, that is to say supercooled liquid water exponentially
 424 increases with temperature in the range -36°C to -16°C. This is in agreement with the outputs
 425 from a simple model for thermodynamic properties of water from sub-zero temperatures up to
 426 +100°C (Sippola and Taskinen, 2018). The model shows that the density ρ (g cm^{-3}) of liquid
 427 water exponentially increases with temperature from -34°C to 0°C through the following
 428 relationship:

$$429 \rho = \rho_0 \exp\{-T_c(A + B\varepsilon_0 + 2C\varepsilon_0^{1/2})\} \quad (15)$$

430 where $\rho_0 = 1.007853 \text{ g cm}^{-3}$, $A = 3.9744 \cdot 10^{-4} \text{ K}^{-1}$, $B = 1.6785 \cdot 10^{-3} \text{ K}^{-1}$, and $C = -7.8165 \cdot 10^{-4} \text{ K}^{-1}$;
 431 T_c is the critical temperature (K) and ε_0 (unitless) is defined as:

$$432 \varepsilon_0 = \frac{T}{T_c} - 1 \quad (16)$$

433 where T is temperature in K. In thermodynamics, a critical point is the end point of a phase
 434 equilibrium curve. In our study, the liquid-ice boundary terminates at some critical temperature
 435 T_c . T_c is about 224.8 K if water is pure and free of nucleation nuclei. Sippola and Taskinen
 436 (2018) reviewed a value of $T_c \sim 227\text{-}228 \text{ K}$ (approx. -45°C) in the literature. This is also in

Mis en forme : Retrait : Première ligne : 0,5 cm, Interligne : Double

Mis en forme : Interligne : Double

437 agreement with the results from our study showing that, above Concordia, we could not
 438 observed SLWCs at temperatures less than -36°C consistent with the fact that the threshold
 439 temperature to get SLWCs should be around -39°C (see the discussions on errors in section
 440 5.3).

441 Note that the relationships show an exponential dependence of LWP on both temperature
 442 and SR anomaly. Similarly, the density ρ (g cm^{-3}) and molar volume v ($\text{cm}^3 \text{mol}^{-1}$) of liquid
 443 water are exponentially varying with temperature (Sippola and Taskinen, 2018):

$$\rho = \rho_0 \exp\left\{-\frac{T}{T_e}(A + B\epsilon_0 + 2C\epsilon_0^{1/2})\right\} \quad (15)$$

$$v = \frac{M_{H_2O}}{\rho} = \frac{M_{H_2O}}{\rho_0} \exp\left\{\frac{T}{T_e}(A + B\epsilon_0 + 2C\epsilon_0^{1/2})\right\} \quad (16)$$

446 where ρ_0 (g cm^{-3}), A (K^{-1}), B (K^{-1}), and C (K^{-1}) are parameters; T_e is the critical temperature
 447 whose value varies from 227 to 228 K, and M_{H_2O} (g mol^{-1}) is the molecular weight of water.
 448 ϵ_0 (unitless) is defined as:

$$\epsilon_0 = \frac{T}{T_e} - 1 \quad (17)$$

450 where T is temperature in K.

451 5.2. Modelling SLWC

452 Previous studies have already underlined the difficulty to model the SLWC together with
 453 its impact on surface radiations. Modelling SLWCs over Antarctica is challenging because 1)
 454 operational observations are scarce since the majority of meteorological radiosondes are
 455 released from ground stations located at the coast and very few of them are maintained all year
 456 long, and satellite observations are limited to 60°S in geostationary orbit whilst, in a polar orbit,
 457 the number of available orbits does not exceed 15 per day, and 2) the model should provide a
 458 partition function favouring liquid water at the expense of ice for temperatures between -36°C
 459 and 0°C in order to calculate realistic SLW contents. Differences of 20 to 50 W m^{-2} in the **Net**
 460 **net** surface irradiance were found in the Arpege model (Pailleux et al., 2015) between clouds

461 made of ice or liquid water during the summer 2018-2019 (Ricaud et al., 2020), differences that
462 are very consistent with the results obtained in the present study. Although SLWCs are less
463 present over the Antarctic Plateau than over the coastal region, their radiative impact is not
464 negligible and should be taken into account with great care in order to estimate the radiative
465 budget of the Antarctic continent in one hand, and, on the other hand, over the entire Earth.

466 5.3. Errors

467 Measurements of temperature, LWP, depolarization signal and surface irradiances F are
468 altered by random and systematic errors that may affect the relationships we have obtained
469 between LWP and either temperature or cloud radiative forcing ΔF_{net} , ΔF , and its individual
470 components. The temperature measured by HAMSTRAD below 1 km has been evaluated
471 against radiosonde coincident observations from 2009 to 2014 (Ricaud et al., 2015) and the
472 resulting bias is 0- to 2°C below 100 m and between -2 and 0°C between 100 and 1000 m.
473 SLWCs are usually located around 400-600 m above the ground where the cold bias can be
474 estimated to be about -1.0°C. The one-sigma ($1-\sigma$) RMS temperature error over a 7-min
475 integration time is 0.25°C in the PBL and 0.5°C in the free troposphere (Ricaud et al., 2015).
476 As a consequence, given the number of points used in the statistical analysis (>1000), the
477 random error on the weighted-average temperature is negligible (<0.02°C). The LWP random
478 and systematic errors are difficult to evaluate since there is no coincident external data to
479 compare with. Nevertheless, the $1-\sigma$ RMS error over a 7-min integration time can be estimated
480 to be 0.25 g m⁻² giving a random error on the weighted average LWP less than 0.08 g m⁻². Based
481 on clear-sky observations, the positive bias can be estimated to be of the order of 0.4 g m⁻².
482 Theoretically, SLW should not exist at temperatures less than -39°C although it has been
483 observed in recent laboratory measurements down to -42.55°C (Goy et al., 2018). Using
484 equation (13) with an LWP bias of 0.4 g m⁻² gives a temperature of -39.8°C (~0.8°C lower than

485 the theoretical limit of -39°C), so the biases estimated for temperature and LWP are very
486 consistent with theory.

487 The estimation of systematic and random errors on LIDAR backscattering and
488 depolarization signals and their impact on the attribution/selection of SLWC is not trivial. But
489 the most important point is to evaluate whether the observed cloud is constituted of purely liquid
490 or mixed-phase water. Even considering the backscatter intensity only, we could not exclude
491 that ice particles could have been present in the SLWC events investigated in 2018 (Ricaud et
492 al., 2020). Therefore, in the present analysis, although we made a great attention to diagnose
493 ice in the LIDAR cloud observations, we cannot totally exclude ice particles thus mixed-phase
494 parcels were actually present when we labelled the observed cloud as SLWCs.

495 The 4 instruments providing F_{LW}^{Down} , F_{LW}^{Up} , F_{SW}^{Down} , and F_{SW}^{Up} follow the rules of acquisition,
496 quality check and quality control of the BSRN (Driemel et al., 2018). These data are often
497 considered as a reference against which products based on satellite observations and radiative
498 transfer models (such as e.g. CERES) are validated (Kratz et al., 2020). In polar regions
499 (Lanconelli et al., 2011), F_{SW}^{Down} and F_{SW}^{Up} are expected to be affected by random errors up to
500 $\pm 20 \text{ W m}^{-2}$ while F_{LW}^{Down} are expected to be affected by random errors not greater than $\pm 10 \text{ W}$
501 m^{-2} (Ohmura et al., 1998). As a consequence, given the large number of observations used per
502 5 W m^{-2} -wide bins (1000-3000), the random error on the weighted-average F is negligible (0.3-
503 to 0.7 W m^{-2}) whatever the radiations considered, LW and SW.

504 Finally, another source of error comes from 1) the geometry of observation and 2) the
505 discontinuous SLWC layer. Firstly, LIDAR is almost zenith pointing, HAMSTRAD makes a
506 scan in the East direction (from 10° elevation to zenith), whilst the BSRN radiometers detect
507 the radiation in a 2π -steradians field of view (3D configuration). That is to say, in our analysis,
508 the whole sky contributes to the radiation whilst only the cloud at zenith (1D configuration) and
509 on the East direction (2D configuration) is observed by the LIDAR and HAMSTRAD,

510 respectively. Secondly, SLWCs cannot be considered as uniform in the whole (see e.g. broken
511 cloud fields in Figure 2).

512 *5.4. Other clouds*

513 Although the method we have developed to select the SLWCs has been validated using the
514 amount of LWP and, in another study, using space-borne observations (Ricaud et al., 2020), we
515 cannot rule out that, associated with the SLW droplets, are also ice particles, that is clouds are
516 constituted of a mixture of liquid and solid water. Statistics of ice and mixed-phase clouds over
517 the Antarctic Plateau have been performed by Cossich et al. (2021) revealing mean annual
518 occurrences of 72.3 %, 24.9 %, and 2.7 % for clear sky, ice clouds, and mixed-phase clouds,
519 respectively. Generally, mixed-phase clouds are a superposition of a lower layer being made of
520 liquid water and an upper layer being made of solid water (see Fig. 12.3 from Lamb and
521 Verlinde, 2011). These mixed-layer clouds do not significantly modify the relationship between
522 temperature and LWP because 1) SLW observations from HAMSTRAD are only sensitive to
523 water in liquid phase and 2) temperature from HAMSTRAD is selected at times and vertical
524 heights where the LIDAR depolarization signal is very low (<5%). Although we have verified
525 that pure ice clouds were not selected by our method, we cannot differentiate mixed-phase
526 clouds from purely SLWCs.

527 Furthermore, we already have noticed that SLWCs developed at the top of the PBL (Ricaud
528 et al., 2020) in the “entrainment zone” and maintained in the “capping inversion zone”,
529 following the terminology of Stull (1988), at a height ranging from 100 to 1000 m above ground
530 level. Nevertheless, at 00:00-06:00 LT when the sun is at low elevation above the horizon (24-
531 h polar day), the PBL may collapse down to a very low height ranging 20-50 m. In this
532 configuration, it is hard to differentiate from LIDAR observations between a SLWC and a fog
533 episode, although the LIDAR can measure depolarization (but not backscatter) down to

534 approximately 10-30 m above the ground (Figure S3 in Chen et al., 2017), so that we can
535 distinguish liquid/frozen clouds very close to the ground.

536 Finally, we cannot rule out that, above the SLWCs that are actually observed by both
537 LIDAR and HAMSTRAD, other clouds might be present, as e.g. cirrus clouds constituted of
538 ice crystals. These mid-to-upper tropospheric clouds cannot be detected by HAMSTRAD (no
539 sensitivity to ice crystals). In the presence of SLWCs either low in altitude or optically thick,
540 the LIDAR backscatter signal is decreased in order to avoid saturation and the signal from upper
541 layers is thus almost cancelled. These mid-to-high-altitude clouds are sensed by the BSRN
542 instruments and surface irradiance can be affected in this configuration. Based on the presence
543 of cirrus clouds before or after the SLWCs (and sometimes during the SLWCs if optically thin),
544 we can estimate that the number of days when SLWCs and cirrus clouds are simultaneously
545 present to cover less than 10% of our period of interest.

546 5.5. Sastrugi effect on the surface albedo

547 Sastrugi (~~Figure 10~~) are features formed by erosion of snow by wind. They are found in
548 polar regions, and in snowy, wind-swept areas of temperate regions, such as frozen lakes or
549 mountain ridges. Sastrugi are distinguished by upwind-facing points, resembling anvils, which
550 move downwind as the surface erodes.

551 Figure ~~4~~10 shows the BSRN surface albedo averaged over the five cloud-free days (2
552 and 19 December 2018; 3, 17 and 26 December 2021) showing a clear diurnal signal with a
553 maximum of 0.85 from 10:00 to 14:00 UTC (from 18:00 to 22:00 LT) and a minimum of 0.70
554 from 19:00 to 23:00 UTC (from 03:00 to 07:00 LT). The large diurnal signal present in the
555 observed surface albedo is likely the signature of 1) the sastrugi orientation and also 2) the sun
556 zenith angle which impacts on the surface albedo even with a flat snow surface (Gardner and
557 Sharp, 2010). Note that the surface albedo of snow under cloudy conditions may differ from
558 the surface albedo under cloud-free conditions (e.g., Gardner and Sharp, 2010; Stapf et al.,

559 ~~2020). The large diurnal signal present in the observed surface albedo is likely the signature of~~
560 ~~the sastrugi effect.~~ The BSRN F_{SW}^{Up} sensor has a circular footprint. For a sensor installed
561 at a height h above the ground, 90% of the signal comes from an area at the surface closer than
562 $3.1 h$ (Kassianov et al., 2014). Since at Dome-C the instrument is installed at a height of 2-3 m,
563 the albedo is thus determined by the surface elements in the immediate vicinity (a few meters)
564 of the sensor.

565 We have fitted the averaged cloud-free BSRN surface albedo with the sum of two sine
566 functions, imposing periods of 24 and 12 hours (Figure ~~4210~~ [4110](#)) together with the residuals
567 between the averaged surface albedo and the fitted function. We can state that the sastrugi effect
568 on the observed cloud-free surface albedo at Concordia is successfully fitted by two sine
569 functions of 24h and 12h periods to within 0.003 mean absolute error, with a coefficient of
570 determination R^2 equal to 0.993 and a root mean square error of 0.0004.

571 Moreover, we have considered all the BSRN observations in Decembers 2018, 2019, 2020
572 and 2021 to calculate the albedo (Figure ~~4211~~ [4111](#)), and we have superimposed the fitted
573 trigonometric function as described in Figure [4110](#). The presence of clouds is well highlighted
574 by observations that depart from the fitted function whilst, during periods of clear-sky
575 conditions, BSRN albedos coincide well with the fitted function. To conclude, the surface
576 albedo at Concordia should be treated considering sastrugi effect.

577 5.6. Maximum SLWC Radiative Forcing over Antarctica

578 Based on 2007-2010 reanalyses, observations and climate models (Lenaerts et al., 2017),
579 LWP over Antarctica is on average less than 10 g m^{-2} , with slightly larger values in summer
580 than in winter by ~~2- to~~ [2- to](#) 5 g m^{-2} . Over Western Antarctica, LWPs are larger (~~20- to~~ [20- to](#) 40 g m^{-2}) than
581 over Eastern Antarctica (~~0- to~~ [0- to](#) 10 g m^{-2}). As a consequence, LWPs observed at Concordia are
582 consistent with values observed over the Eastern Plateau, with a factor ~~2- to~~ [2- to](#) 4 smaller than those
583 observed over the Western continent. Based on our results and on the observed cloud fraction

584 (η_{CF}) of SLWCs over Antarctica for different seasons (Listowski et al., 2019), we can estimate
585 the maximum SLWC radiative forcing at the scale of the Antarctic continent ($\Delta F_{Net-Ant}^{max}$) from
586 the maximum of ΔF_{net} ($\Delta F_{Net}^{max} = 70 \text{ W m}^{-2}$) computed in our study:

$$587 \quad \Delta F_{Net-Ant}^{max} = \eta_{CF} \times \Delta F_{Net}^{max} \quad (17)$$

588 Equation (17) assumes a linear dependence between cloud fraction and cloud radiative forcing
589 although, in nature, there could be three-dimensional radiation effects. In summer, η_{CF} is
590 varying from 5% in Eastern Antarctica to 40% in Western Antarctica whilst, in winter, it is
591 varying from 0% in Eastern Antarctica to 20% in Western Antarctica (Listowski et al., 2019).
592 In December, if we consider η_{CF} for SLW-containing cloud (that is to say both mixed-phase
593 cloud and unglaciated SLW cloud consistent with our study), we find for a lower-level altitude
594 cut-off of 0, 500 and 1000 m (Figure B1 in Listowski et al., 2019), a maximum SLWC radiative
595 forcing $\Delta F_{Net-Ant}^{max}$ over Antarctica of about 12 W m^{-2} , 10 W m^{-2} and 7 W m^{-2} , respectively. We
596 now separate the Eastern elevated Antarctic Plateau from the Western Antarctica (Figure 5 in
597 Listowski et al., 2019) for the 4 seasons. Over Eastern Antarctica, we find that $\Delta F_{Net-Ant}^{max} =$
598 0.7-to 7.0 W m^{-2} in December-January-February (DJF) and 0-to 3.5 W m^{-2} for the remaining
599 seasons. Over Western Antarctica, the maximum radiative impact is much more intense because
600 of higher temperatures and lower elevations compared to the Eastern Antarctic Plateau:
601 $\Delta F_{Net-Ant}^{max} =$ 17.5-to 40.0 W m^{-2} in DJF (40 W m^{-2} over the Antarctica Peninsula); 10.5-to
602 28.0 W m^{-2} in March-April-May; 3.5-to 14.0 W m^{-2} in June-July-August; and 7.0-to 17.5 W
603 m^{-2} in September-October-November. To summarize, the maximum SLWC radiative forcing
604 over Western Antarctica (0-to 40 W m^{-2}) is estimated to 3 to 5 times larger compared to the
605 one over the Eastern Antarctic Plateau (0-to 7 W m^{-2}), maximizing during the summer season.

606

607 **6. Conclusions**

608 Combining the observations of temperature, water vapour and liquid water path from a
609 ground-based microwave radiometer, backscattering and depolarization from a ground-based
610 LIDAR, screen-level air temperature and surface radiations at long and short wavelengths, our
611 analysis has been able to evaluate the presence of supercooled liquid water clouds over the
612 Dome C station in summer. Focusing on the month of December in 2018-2021, we established
613 that in SLWCs temperature logarithmically increases from -36.0°C to -16.0°C when LWP
614 increases from 1.0 to 14.0 g m^{-2} . We have also evaluated that SLWCs have a positive cloudly
615 affect the net-radiative forcing, which logarithmically increases from 0.0 to 70.0 W m^{-2} when
616 LWP increases from 1.2 to 3.5 g m^{-2} . Our study clearly shows that SLWCs have a positive
617 impact on ΔF_{LW}^{Down} increasing from 0 to 90 W m^{-2} for LWP ranging from 1.0 to 3.5 g m^{-2} , a
618 negligible impact ($\pm 5\text{ W m}^{-2}$) on ΔF_{LW}^{Up} for LWP ranging from 0 to 6.5 g m^{-2} , and a negative
619 (but quite offsetting) impact on each of the two terms ΔF_{SW}^{Down} and ΔF_{SW}^{Up} which decrease from
620 0 to -130 and -110 W m^{-2} , respectively for LWP ranging from 1.5 to 4.0 g m^{-2} . This means that
621 the impact of SLWC on the net-radiative forcing is mainly driven by the downward surface
622 irradiance since the attenuation of shortwavesolar incoming irradiance is almost compensated
623 for by the upward shortwave irradiance because of high values of surface albedo.

624 Finally, extrapolating our results of the SLWC radiative forcing from the Dome C station
625 to the Antarctic continent shows that the maximum SLWC radiative forcing is not greater than
626 7.0 W m^{-2} over the Eastern Antarctic Plateau but 2 to 3 times larger (up to 40 W m^{-2}) over
627 Western Antarctica, maximizing over in summer season and over the Antarctic Peninsula. This
628 stresses the importance of accurately modelling SLWCs when calculating the Earth energy
629 budget to adequately forecast the Earth climate evolution, especially since the climate is rapidly
630 changing in Antarctica, as illustrated by the surface temperature record of -12°C recently
631 observed in March 2022 at the Concordia station and largely publicized worldwide (see e.g.

632 [https://www.9news.com.au/world/antarctica-heatwave-extreme-warm-weather-recorded-](https://www.9news.com.au/world/antarctica-heatwave-extreme-warm-weather-recorded-concordia-research-station/3364dd91-2051-4df5-8cfc-5f2819058604)
633 [concordia-research-station/3364dd91-2051-4df5-8cfc-5f2819058604](https://www.9news.com.au/world/antarctica-heatwave-extreme-warm-weather-recorded-concordia-research-station/3364dd91-2051-4df5-8cfc-5f2819058604)).

634

635 **Data availability**

636 HAMSTRAD data are available at <http://www.cnrn.meteo.fr/spip.php?article961&lang=en>
637 (last access: ~~3 May~~[27 November 2022](#)~~2023~~). The tropospheric depolarization LIDAR data are
638 reachable at <http://lidarmax.altervista.org/lidar/home.php> (last access: ~~27 November 2023~~
639 ~~May 2022~~). Radiosondes are available at <http://www.climantartide.it> (last access: ~~27~~
640 ~~November 2023~~~~May 2022~~). Screen-level air temperature from AWS can be obtained from
641 the ftp server (<https://amrc.ssec.wisc.edu/data/archiveaws.html>) (last access: ~~27 November~~
642 ~~2023~~~~17 October 2023~~). BSRN data can be obtained from the ftp server
643 (<https://bsrn.awi.de/data/data-retrieval-via-ftp/>) (last access: ~~27 November 2023~~~~May 2022~~).

644

645 **Author contribution**

646 PR, MDG, and AL provided the observational data. PR developed the methodology. All the
647 co-authors participated in the data analysis and in the data interpretation. PR prepared the
648 manuscript with contributions from all co-authors.

649

650 **Competing interests**

651 The authors declare that they have no conflict of interest.

652

653 **Acknowledgments**

654 The present research project Water Budget over Dome C (H2O-DC) has been approved by
655 the Year of Polar Prediction (YOPP) international committee. The HAMSTRAD programme
656 (910) was supported by the French Polar Institute, Institut polaire français Paul-Emile Victor

657 (IPEV), the Institut National des Sciences de l'Univers (INSU)/Centre National de la Recherche
658 Scientifique (CNRS), Météo-France and the Centre National d'Etudes Spatiales (CNES). The
659 permanently manned Concordia station is jointly operated by IPEV and the Italian Programma
660 Nazionale Ricerche in Antartide (PNRA). The tropospheric LIDAR operates at Dome C from
661 2008 within the framework of several Italian national (PNRA) projects. We would like to thank
662 all the winterover personnel who worked at Dome C on the different projects: HAMSTRAD,
663 aerosol LIDAR and BSRN. We would like to thank the three anonymous reviewers for their
664 beneficial comments.

665

666 **References**

- 667 Bergeron, T., 1928: Über die dreidimensional verknüpfende Wetteranalyse. – *Geophys. Norv.*
- 668 Branch, M. A., T. F. Coleman, and Y. Li: A Subspace, Interior, and Conjugate Gradient Method
669 for Large-Scale Bound-Constrained Minimization Problems, *SIAM Journal on Scientific*
670 *Computing*, 21, 1, 1-23, 1999.
- 671 Bromwich, D. H., Nicolas, J. P., Hines, K. M., Kay, J. E., Key, E. L., Lazzara, Lubin, D.,
672 McFarquhar, G. M., Gorodetskaya, I. V., Grosvenor, D. P., Lachlan-Cope, T., and van
673 Lipzig, N. P. M.: Tropospheric clouds in Antarctica, *Rev. Geophys.*, 50, RG1004,
674 <https://doi.org/10.1029/2011RG000363>, 2012.
- 675 Bromwich, D. H., Otieno, F. O., Hines, K. M., Manning, K. W., and Shilo, E.: Comprehensive
676 evaluation of polar weather research and forecasting model performance in the Antarctic, *J.*
677 *Geophys. Res.-Atmos.*, 118, 274–292, 2013.
- 678 Chen, X., Virkkula, A., Kerminen, V.-M., Manninen, H. E., Busetto, M., Lanconelli, C., Lupi,
679 A., Vitale, V., Del Guasta, M., Grigioni, P., Väänänen, R., Duplissy, E.-M., Petäjä, T., and
680 Kulmala, M.: Features in air ions measured by an air ion spectrometer (AIS) at Dome C,
681 *Atmos. Chem. Phys.*, 17, 13783–13800, <https://doi.org/10.5194/acp-17-13783-2017>, 2017.

682 Cossich, W., Maestri, T., Magurno, D., Martinazzo, M., Di Natale, G., Palchetti, L., Bianchini,
683 G., and Del Guasta, M.: Ice and mixed-phase cloud statistics on the Antarctic Plateau,
684 *Atmos. Chem. Phys.*, 21, 13811–13833, <https://doi.org/10.5194/acp-21-13811-2021>, 2021.

685 Driemel, A., Augustine, J., Behrens, K., Colle, S., Cox, C., Cuevas-Agulló, E., Denn, F. M.,
686 Duprat, T., Fukuda, M., Grobe, H., Haeffelin, M., Hodges, G., Hyett, N., Ijima, O., Kallis,
687 A., Knap, W., Kustov, V., Long, C. N., Longenecker, D., Lupi, A., Maturilli, M., Mimouni,
688 M., Ntsangwane, L., Ogihara, H., Olano, X., Olefs, M., Omori, M., Passamani, L., Pereira,
689 E. B., Schmihüsen, H., Schumacher, S., Sieger, R., Tamlyn, J., Vogt, R., Vuilleumier, L.,
690 Xia, X., Ohmura, A., and König-Langlo, G.: Baseline Surface Radiation Network (BSRN):
691 structure and data description (1992–2017), *Earth Syst. Sci. Data*, 10, 1491–1501,
692 <https://doi.org/10.5194/essd-10-1491-2018>, 2018.

693 Dupont, J.C., Haeffelin, M., Drobinski, P. and Besnard, T.: Parametric model to estimate clear-
694 sky longwave irradiance at the surface on the basis of vertical distribution of humidity and
695 temperature. *Journal of Geophysical Research: Atmospheres*, 113(D7),
696 <https://doi.org/10.1029/2007JD009046>, 2008.

697 Dutton, E.G., Farhadi, A., Stone, R.S., Long, C.N. and Nelson, D.W.: Long-term variations in
698 the occurrence and effective solar transmission of clouds as determined from surface-based
699 total irradiance observations. *Journal of Geophysical Research: Atmospheres*, 109(D3),
700 <https://doi.org/10.1029/2003JD003568>, 2004.

701 Findeisen, W., 1938: Kolloid-meteorologische Vorgänge bei Niederschlagsbildung. *Meteorol.*
702 *Z.* 55, 121–133. (translated and edited by Volken, E., A.M. Giesche, S. Brönnimann. –
703 *Meteorol. Z.* 24 (2015), DOI:10.1127/metz/2015/0675).

704 Gardner, A.S. and Sharp, M.J.: A review of snow and ice albedo and the development of a new
705 physically based broadband albedo parameterization. *Journal of Geophysical Research:*
706 *Earth Surface*, 115(F1), 2010.

707 Goy, C., Potenza, M. A., Dedera, S., Tomut, M., Guillermin, E., Kalinin, A., Voss, K.-O.,
708 Schottelius, A., Petridis, N., Prosvetov, A., Tejada, G., Fernández, J. M., Trautmann, C.,
709 Caupin, F., Glasmacher, U., and Grisenti, R. E.: Shrinking of rapidly evaporating water
710 microdroplets reveals their extreme supercooling, *Phys. Rev. Lett.*, 120, 015501,
711 <https://doi.org/10.1103/PhysRevLett.120.015501>, 2018.

712 Grazioli, J., Genthon, C., Boudevillain, B., Duran-Alarcon, C., Del Guasta, M., Madeleine, J.-
713 B., and Berne, A.: Measurements of precipitation in Dumont d’Urville, Adélie Land, East
714 Antarctica, *The Cryosphere*, 11, 1797–1811, <https://doi.org/10.5194/tc-11-1797-2017>,
715 2017.

716 Grosvenor, D. P., Choularton, T. W., Lachlan-Cope, T., Gallagher, M. W., Crosier, J., Bower,
717 K. N., Ladkin, R. S., and Dorsey, J. R.: In-situ aircraft observations of ice concentrations
718 within clouds over the Antarctic Peninsula and Larsen Ice Shelf, *Atmos. Chem. Phys.*, 12,
719 11275–11294, <https://doi.org/10.5194/acp-12-11275-2012>, 2012.

720 Hogan, R. J. and Illingworth, A. J.: The effect of specular reflection on spaceborne lidar
721 measurements of ice clouds, Report of the ESA Retrieval algorithm for EarthCARE project,
722 5 pp., 2003.

723 Kassianov E, Barnard J, Flynn C, Riihimaki L, Michalsky J, Hodges G (2014) Areal-averaged
724 spectral surface albedo from ground-based transmission data alone: toward an operational
725 retrieval. *Atmosphere* 5:597–621. <https://doi.org/10.3390/atmos503059>

726 King, J. C., Argentini, S. A., and Anderson, P. S.: Contrasts between the summertime surface
727 energy balance and boundary layer structure at Dome C and Halley stations, Antarctica, *J.*
728 *Geophys. Res.-Atmos.*, 111, D02105, <https://doi.org/10.1029/2005JD006130>, 2006.

729 King, J. C., Gadian, A., Kirchgaessner, A., Kuipers Munneke, P., Lachlan-Cope, T. A., Orr, A.,
730 Reijmer, C., Broeke, M. R., van Wessem, J. M., and Weeks, M.: Validation of the
731 summertime surface energy budget of Larsen C Ice Shelf (Antarctica) as represented in

732 three high-resolution atmospheric models, *J. Geophys. Res.-Atmos.*, 120, 1335–1347,
733 <https://doi.org/10.1002/2014JD022604>, 2015.

734 Kratz, D. P., Gupta, S. K., Wilber, A. C., and Sothcott, V. E.: Validation of the CERES Edition-
735 4A Surface-Only Flux Algorithms, *J. Appl. Meteorol. Clim.*, 59, 281–295,
736 <https://doi.org/10.1175/JAMC-D-19-0068.1>, 2020.

737 Lachlan-Cope, T.: Antarctic clouds, *Polar Res.*, 29, 150–158, 2010.

738 Lachlan-Cope, T., Listowski, C., and O’Shea, S.: The microphysics of clouds over the Antarctic
739 Peninsula – Part 1: Observations, *Atmos. Chem. Phys.*, 16, 15605–15617,
740 <https://doi.org/10.5194/acp-16-15605-2016>, 2016.

741 Lamb, D., and J. Verlinde: *Physics and chemistry of clouds*. Cambridge University Press, 2011.

742 Lanconelli, C., Busetto, M., Dutton, E. G., König-Langlo, G., Maturilli, M., Sieger, R., Vitale,
743 V., and Yamanouchi, T.: Polar baseline surface radiation measurements during the
744 International Polar Year 2007–2009, *Earth Syst. Sci. Data*, 3, 1–8,
745 <https://doi.org/10.5194/essd-3-1-2011>, 2011.

746 Lawson, R. P. and Gettelman, A.: Impact of Antarctic mixed-phase clouds on climate, *P. Natl.*
747 *Acad. Sci. USA*, 111, 18156–18161, 2014.

748 Legrand, M., Yang, X., Preunkert, S., and Therys, N.: Year-round records of sea salt, gaseous,
749 and particulate inorganic bromine in the atmospheric boundary layer at coastal (Dumont
750 d’Urville) and central (Concordia) East Antarctic sites, *J. Geophys. Res. Atmos.*, 121, 997–
751 1023, <https://doi.org/10.1002/2015JD024066>, 2016.

752 Lemus, L., Rikus, L., Martin, C., and Platt, R.: Global cloud liquid water path simulations. *J.*
753 *Climate*, 10(1), 52-64, 1997.

754 Lenaerts, J. T., Van Tricht, K., Lhermitte, S. and L’Ecuyer, T. S.: Polar clouds and radiation in
755 satellite observations, reanalyses, and climate models, *Geophysical Research Letters*, 44(7),
756 3355-3364, 2017.

757 Listowski, C. and Lachlan-Cope, T.: The microphysics of clouds over the Antarctic Peninsula
758 – Part 2: modelling aspects within Polar WRF, *Atmos. Chem. Phys.*, 17, 10195–10221,
759 <https://doi.org/10.5194/acp-17-10195-2017>, 2017.

760 Listowski, C., Delanoë, J., Kirchgaessner, A., Lachlan-Cope, T., and King, J.: Antarctic clouds,
761 supercooled liquid water and mixed phase, investigated with DARDAR: geographical and
762 seasonal variations, *Atmos. Chem. Phys.*, 19, 6771–6808, [https://doi.org/10.5194/acp-19-](https://doi.org/10.5194/acp-19-6771-2019)
763 [6771-2019](https://doi.org/10.5194/acp-19-6771-2019), 2019.

764 Lubin, D., Chen, B., Bromwich, D. H., Somerville, R. C., Lee, W. H., and Hines, K. M.: The
765 Impact of Antarctic Cloud Radiative Properties on a GCM Climate Simulation, *J. Climate*,
766 11, 447-462, 1998.

767 Mishchenko, M. I., Hovenier, J. W., and Travis, L. D. (Eds.): *Light Scattering by Nonspherical*
768 *Particles: Theory, Measurements, and Applications*, Academic Press, chap. 14, 393–416,
769 2000.

770 Ohmura, A., Dutton, E. G., Forgan, B., Fröhlich, C., Gilgen, H., Hegner, H., Heimo, A., König-
771 Langlo, G., McArthur, B., Müller, G., Philipona, R., Pinker, R., Whitlock, C. H., Dehne,
772 K., and Wild, M.: Baseline Surface Radiation Network (BSRN/WCRP): New precision
773 radiometry for climate research, *B. Am. Meteorol. Soc.*, 79(10), 2115-2136, 1998.

774 O’Shea, S. J., Choulaton, T. W., Flynn, M., Bower, K. N., Gallagher, M., Crosier, J., Williams,
775 P., Crawford, I., Fleming, Z. L., Listowski, C., Kirchgaessner, A., Ladkin, R. S., and
776 Lachlan-Cope, T.: In situ measurements of cloud microphysics and aerosol over coastal
777 Antarctica during the MAC campaign, *Atmos. Chem. Phys.*, 17, 13049–13070,
778 <https://doi.org/10.5194/acp-17-13049-2017>, 2017.

779 Pailleux, J., Geleyn, J.-F., El Khatib, R., Fischer, C., Hamrud, M., Thépaut, J.-N., Rabier, F.,
780 Andersson, E., Salmond, D., Burridge, D., Simmons, A., and Courtier, P.: Les 25 ans du

781 système de prévision numérique du temps IFS/Arpège, *La Météorologie*, 89, 18–27,
782 <https://doi.org/10.4267/2042/56594>, 2015.

783 Ricaud, P., Gabard, B., Derrien, S., Chaboureaud, J.-P., Rose, T., Mombauer, A. and Czekala,
784 H.: HAMSTRAD-Tropo, A 183-GHz Radiometer Dedicated to Sound Tropospheric Water
785 Vapor Over Concordia Station, Antarctica, *IEEE T. Geosci. Remote*, 48, 1365–1380, doi:
786 10.1109/TGRS.2009.2029345, 2010a.

787 Ricaud, P., Gabard, B., Derrien, S., Attié, J.-L., Rose, T., and Czekala, H.: Validation of
788 tropospheric water vapor as measured by the 183-GHz HAMSTRAD Radiometer over the
789 Pyrenees Mountains, France, *IEEE T. Geosci. Remote*, 48, 2189–2203, 2010b.

790 Ricaud, P., Genthon, C., Durand, P., Attié, J.-L., Carminati, F., Canut, G., Vanacker, J.-F.,
791 Moggio, L., Courcoux, Y., Pellegrini, A., and Rose, T.: Summer to Winter Diurnal
792 Variabilities of Temperature and Water Vapor in the lowermost troposphere as observed by
793 the HAMSTRAD Radiometer over Dome C, Antarctica, *Bound.-Lay. Meteorol.*, 143, 227–
794 259, doi:10.1007/s10546-011-9673-6, 2012.

795 Ricaud, P., Grigioni, P., Zbinden, R., Attié, J.-L., Genoni, L., Galeandro, A., Moggio, A.,
796 Montaguti, S., Petenko, I., and Legovini, P.: Review of tropospheric temperature, absolute
797 humidity and integrated water vapour from the HAMSTRAD radiometer installed at Dome
798 C, Antarctica, 2009–14, *Antarct. Sci.*, 27, 598–616, doi:10.1017/S0954102015000334,
799 2015.

800 Ricaud, P., Bazile, E., del Guasta, M., Lanconelli, C., Grigioni, P., and Mahjoub, A.: Genesis
801 of diamond dust, ice fog and thick cloud episodes observed and modelled above Dome C,
802 Antarctica, *Atmos. Chem. Phys.*, 17, 5221–5237, [https://doi.org/10.5194/acp-17-5221-](https://doi.org/10.5194/acp-17-5221-2017)
803 2017, 2017.

804 Ricaud, P., Del Guasta, M., Bazile, E., Azouz, N., Lupi, A., Durand, P., Attié, J.-L., Veron, D.,
805 Guidard, V., and Grigioni, P.: Supercooled liquid water cloud observed, analysed, and

806 modelled at the top of the planetary boundary layer above Dome C, Antarctica, Atmos.
807 Chem. Phys., 20, 4167–4191, <https://doi.org/10.5194/acp-20-4167-2020>, 2020.

808 Sippola, H., and Taskinen, P.: Activity of supercooled water on the ice curve and other
809 thermodynamic properties of liquid water up to the boiling point at standard pressure, J.
810 Chem. Engineer. Data, 63(8), 2986-2998, 2018.

811 [Stapf, J., Ehrlich, A., Jäkel, E., Lüpkes, C., and Wendisch, M.: Reassessment of shortwave](#)
812 [surface cloud radiative forcing in the Arctic: consideration of surface-albedo–cloud](#)
813 [interactions, Atmos. Chem. Phys., 20, 9895–9914, \[https://doi.org/10.5194/acp-20-9895-\]\(https://doi.org/10.5194/acp-20-9895-2020\)](#)
814 [2020, 2020.](#)

815 Storelvmo, T. and Tan, I.: The Wegener–Bergeron–Findeisen process—Its discovery and vital
816 importance for weather and climate, Meteor. Z, 24, 455-461, 2015.

817 Stull, R. B.: An introduction to boundary layer meteorology, Kluwer Academic Publisher,
818 1988.

819 Tomasi, C., Petkov, B., Mazzola, M., Ritter, C., di Sarra, A., di Iorio, T., and del Guasta, M.:
820 Seasonal variations of the relative optical air mass function for background aerosol and thin
821 cirrus clouds at Arctic and Antarctic sites, Remote Sensing, 7(6), 7157-7180, 2015.

822 Wegener, A. 1911. Thermodynamik der Atmosphäre. – Leipzig, Germany: Barth.

823 Wille, J. D., Favier, V., Dufour, A., Gorodetskaya, I. V., Turner, J., Agosta, C. and Codron, F.:
824 West Antarctic surface melt triggered by atmospheric rivers, Nature Geoscience, 12(11),
825 911-916, 2019.

826 Young, G., Lachlan-Cope, T., O’Shea, S. J., Dearden, C., Listowski, C., Bower, K. N.,
827 Choulaton, T. W., and Gallagher, M. W.: Radiative effects of secondary ice enhancement
828 in coastal Antarctic clouds, Geophys. Res. Lett., 46, 2312–2321,
829 <https://doi.org/10.1029/2018GL080551>, 2019.

830

831

Tables

832 **Table 1.** Cloud-free periods in December 2018-2021 detected from the LIDAR depolarization
 833 observations at Concordia. Time is in UTC. MM-NN means from MM (included) hour UTC to
 834 NN (excluded) hour UTC. "X" means no cloud-free period during that day. "ND" means no
 835 LIDAR data available. ~~Greyish-Bold~~ cases mean that cloud-free irradiance calculations are
 836 impossible due to lack of some data (LIDAR, HAMSTRAD, BSRN or AWS).

Days	2018	2019	2020	2021
01	0-24	9-18	ND	9-16
02	0-21	13-17	ND	7-8
03	0-24	6-16	ND	6-24
04	X	11-16	ND	0-24
05	X	6-16	3-16	12-19
06	3-6	0-13	9-13	2-12
07	1-16	X	X	0-24
08	3-15	X	1-2	0-10
09	2-16	X	4-14	10-17
10	0-3	X	X	ND
11	X	4-17	0-1	ND
12	X	X	20-22	ND
13	11-13	10-14	0-12	X
14	22-24	17-18	X	5-12 & 17-20
15	4-8	22-23	X	3-6
16	15-18	X	6-8	11-24
17	18-19	ND	X	0-24
18	1-17	ND	16-17	0-3
19	0-24	ND	7-9 & 11-13	20-23
20	0-12	ND	20-22	16-19
21	X	ND	20-21	X
22	9-16	ND	ND	12-15
23	1-4	ND	14-20	X
24	X	ND	11-14	0-6
25	X	ND	9-15	20-24
26	12-18	ND	0-16 & 18-22	0-24
27	10-11	ND	0-2	0-4
28	0-6	ND	0-17	10-14
29	X	ND	0-18	X
30	X	ND	7-24	X
31	10-12	ND	0-18	X

837

838

- Tableau mis en forme ... [1]
- Mis en forme ... [2]
- Mis en forme ... [3]
- Mis en forme ... [4]
- Mis en forme ... [5]
- Mis en forme ... [6]
- Mis en forme ... [7]
- Mis en forme ... [8]
- Mis en forme ... [9]
- Mis en forme ... [10]
- Mis en forme ... [11]
- Mis en forme ... [12]
- Mis en forme ... [13]
- Mis en forme ... [14]
- Mis en forme ... [15]
- Mis en forme ... [16]
- Mis en forme ... [17]
- Mis en forme ... [18]
- Mis en forme ... [19]
- Mis en forme ... [20]
- Mis en forme ... [21]
- Mis en forme ... [22]
- Mis en forme ... [23]
- Mis en forme ... [24]
- Mis en forme ... [25]
- Mis en forme ... [26]
- Mis en forme ... [27]
- Mis en forme ... [28]
- Mis en forme ... [29]
- Mis en forme ... [30]
- Mis en forme ... [31]
- Mis en forme ... [32]
- Mis en forme ... [33]
- Mis en forme ... [34]
- Mis en forme ... [35]
- Mis en forme ... [36]
- Mis en forme ... [37]
- Mis en forme ... [38]
- Mis en forme ... [39]
- Mis en forme ... [40]
- Mis en forme ... [41]
- Mis en forme ... [42]
- Mis en forme ... [43]
- Mis en forme ... [44]
- Mis en forme ... [45]
- Mis en forme ... [46]
- Mis en forme ... [47]
- Mis en forme ... [48]
- Mis en forme ... [49]
- Mis en forme ... [50]
- Mis en forme ... [51]
- Mis en forme ... [52]
- Mis en forme ... [53]
- Mis en forme ... [54]
- Mis en forme ... [55]
- Mis en forme ... [56]
- Mis en forme ... [57]
- Mis en forme ... [58]
- Mis en forme ... [59]

839

840 **Table 2.** Gaussian functions fitted to the $N(x)$ function for $x = T$ (°C) or ΔF (W m⁻²). Units of

841 $a_1, a_2, a_3,$ and c_0 are in count number for T and ΔF ; units of $\mu_1, \mu_2, \mu_3, \sigma_1, \sigma_2,$ and σ_3 are in

842 °C for T and in W m⁻² for ΔF .

x	a_1	μ_1	σ_1	a_2	μ_2	σ_2	a_3	μ_3	σ_3	c_0
T	$15.0 \cdot 10^3$	-31.5	1.45	$5.0 \cdot 10^3$	-28.0	1.65	$0.5 \cdot 10^3$	-19.0	2.5	$-9.1 \cdot 10^{-6}$
ΔF_{net}	371.7	10.0	11.5	74.6	37.6	21.1	220.8	57.5	14.1	-10.2
ΔF_{LW}^{Down}	415.5	10.0	10.4	189.5	53.7	24.2	227.1	82.9	7.0	-18.5
ΔF_{LW}^{Up}	=	=	=	=	=	=	=	=	=	=
ΔF_{SW}^{Down}	190.5	-10.1	17.2	113.0	-80.0	54.6	=	=	=	-1.9
ΔF_{SW}^{Up}	282.4	-10.1	12.8	133.8	-75.0	41.8	=	=	=	8.3

x	a_1	μ_1	σ_1	a_2	μ_2	σ_2	a_3	μ_3	σ_3	c_0
T	<u>$15.0 \cdot 10^3$</u>	<u>-31.5</u>	<u>1.45</u>	<u>$5.0 \cdot 10^3$</u>	<u>-28.0</u>	<u>1.65</u>	<u>$0.5 \cdot 10^3$</u>	<u>-19.0</u>	<u>2.5</u>	<u>$-9.1 \cdot 10^{-6}$</u>
ΔF_{net}	<u>371.7</u>	<u>10.0</u>	<u>11.5</u>	<u>74.6</u>	<u>37.6</u>	<u>21.1</u>	<u>220.8</u>	<u>57.5</u>	<u>14.1</u>	<u>-10.2</u>
ΔF_{LW}^{Down}	<u>415.5</u>	<u>10.0</u>	<u>10.4</u>	<u>189.5</u>	<u>53.7</u>	<u>24.2</u>	<u>227.1</u>	<u>82.9</u>	<u>7.0</u>	<u>-18.5</u>
ΔF_{LW}^{Up}	<u>=</u>	<u>=</u>	<u>=</u>	<u>=</u>	<u>=</u>	<u>=</u>	<u>=</u>	<u>=</u>	<u>=</u>	<u>=</u>
ΔF_{SW}^{Down}	<u>190.5</u>	<u>-10.1</u>	<u>17.2</u>	<u>113.0</u>	<u>-80.0</u>	<u>54.6</u>	<u>=</u>	<u>=</u>	<u>=</u>	<u>-1.9</u>
ΔF_{SW}^{Up}	<u>282.4</u>	<u>-10.1</u>	<u>12.8</u>	<u>133.8</u>	<u>-75.0</u>	<u>41.8</u>	<u>=</u>	<u>=</u>	<u>=</u>	<u>8.3</u>

← Tableau mis en forme

843

844

845 **Table 3.** Coefficients of the relations $f(LWP) = \alpha + \beta \ln(LWP)$ for the temperature T or
846 cloud radiative forcing ~~components ΔF , (ΔF_{net}) and the individual components (ΔF_{LW}^{Down} ,
847 ΔF_{LW}^{Up} , ΔF_{SW}^{Down} and ΔF_{SW}^{Up})~~. Units of T and ΔF , as well as of their corresponding “ α ” values are
848 in $^{\circ}\text{C}$ and W m^{-2} , respectively; units of β are in $^{\circ}\text{C g}^{-1} \text{m}^2$ for T and in W g^{-1} for ΔF ; units of
849 LWP are in g m^{-2} . The last column shows the range of LWP values for which the relation is
850 valid. $\alpha \pm \delta\alpha$ corresponds to the range of α values where the relationship is valid.

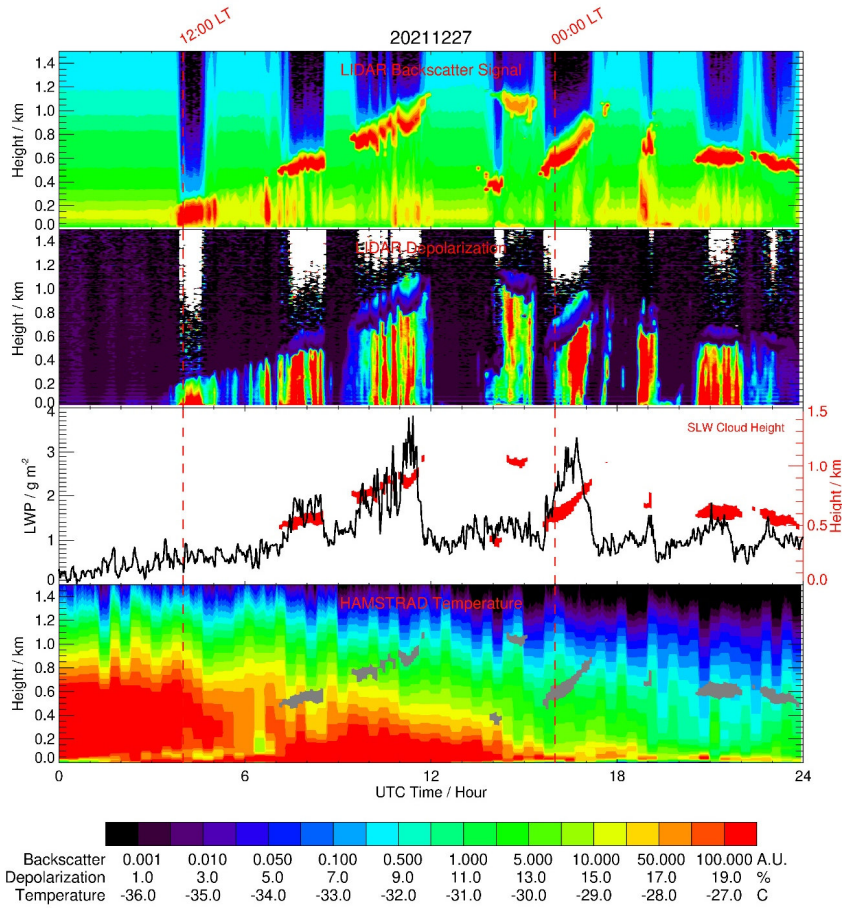
$f(LWP)$	$\alpha \pm \delta\alpha$	β	<u>Valid range</u> for T or ΔF	<u>Valid range</u> for LWP
T	<u>-33.8 ± 1.5</u>	<u>6.5</u>	$[-36; -16]$	$[1.0; 14.0]$
ΔF_{net}	<u>-18.0 ± 10.0</u>	<u>70.0</u>	$[0; 70]$	$[1.2; 3.5]$
ΔF_{LW}^{Down}	<u>5.0 ± 15.0</u>	<u>65.0</u>	$[0; 90]$	$[1.0; 3.5]$
ΔF_{LW}^{Up}	<u>0 ± 5.0</u>	<u>0.0</u>	$[-5; 5]$	$[0.0; 6.5]$
ΔF_{SW}^{Down}	<u>30.0 ± 30.0</u>	<u>-130.0</u>	$[-130; 0]$	$[1.5; 4.0]$
ΔF_{SW}^{Up}	<u>30.0 ± 30.0</u>	<u>-110.0</u>	$[-110; 00]$	$[1.5; 4.0]$
$f(LWP)$	$\alpha \pm \delta\alpha$	β	<u>Valid range</u> for T or ΔF	<u>Valid range</u> for LWP
T	-33.8 ± 1.5	6.5	$[-36; -16]$	$[1.0; 14.0]$
ΔF_{net}	-18.0 ± 10.0	70.0	$[0; 70]$	$[1.2; 3.5]$
ΔF_{LW}^{Down}	5.0 ± 15.0	65.0	$[0; 90]$	$[1.0; 3.5]$
ΔF_{LW}^{Up}	0 ± 5.0	0.0	$[-5; 5]$	$[0.0; 6.5]$
ΔF_{SW}^{Down}	30.0 ± 30.0	-130.0	$[-130; 0]$	$[1.5; 4.0]$
ΔF_{SW}^{Up}	30.0 ± 30.0	-110.0	$[-110; 00]$	$[1.5; 4.0]$

Tableau mis en forme

851

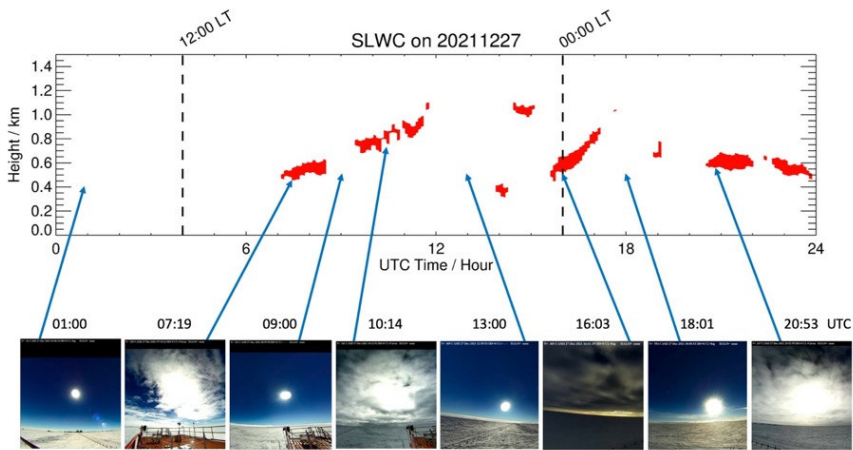
852

Figures



855

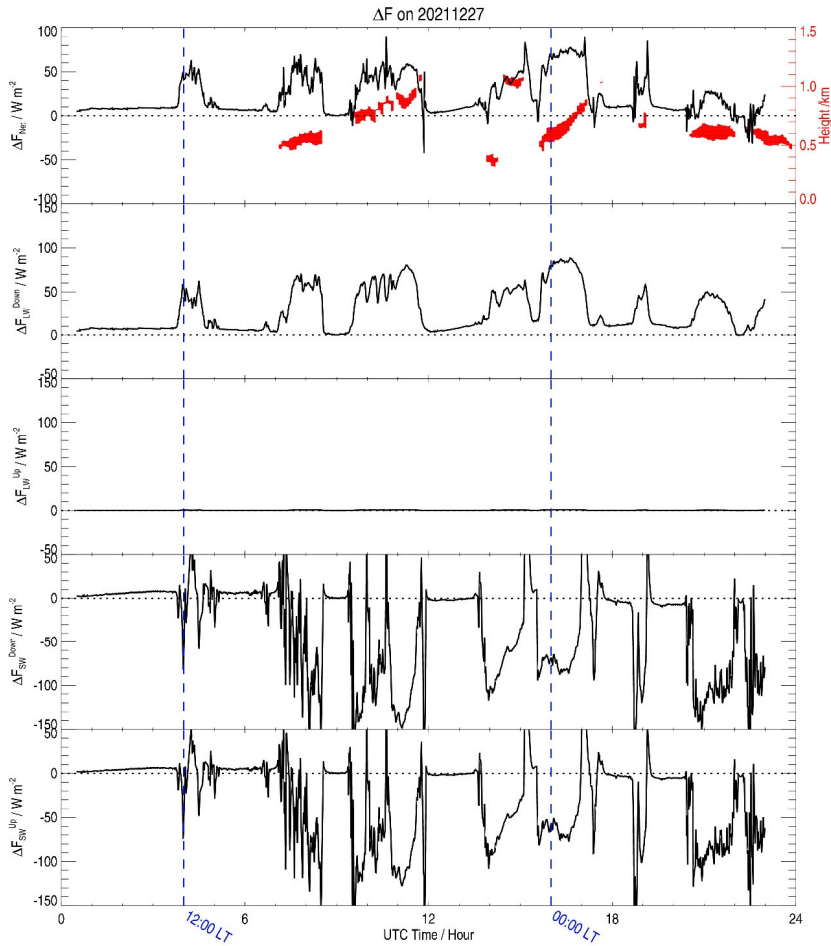
856 **Figure 1:** (From top to bottom): Time evolution (UTC, hour) of the LIDAR backscattering
 857 signal, the LIDAR depolarization signal, the HAMSTRAD LWP and the HAMSTRAD
 858 temperature profile measured on 27 December 2021. The time evolution of the SLW cloud (as
 859 diagnosed by a backscattering value > 60 A.U. and a depolarization value $< 5\%$) is highlighted
 860 by the red and grey areas in the third and the forth panel from the top, respectively. The height
 861 above the ground is shown on the third panel from the top with the y-axis on the right. The
 862 00:00 and 12:00 local times (LT) are highlighted by 2 vertical dashed lines.



863
 864 **Figure 2:** (Top) Time evolution (UTC, hour) of the SLWC (red areas) on 27 December 2021.
 865 (Bottom, from left to right) Snapshots from the HALO-CAM video camera taken on: 01:00 (no
 866 SLWC), 07:19 (SLWC), 09:00 (no SLWC), 10:14 (SLWC), 13:00 (no SLWC), 16:03 (SLWC),
 867 18:01 (no SLWC) and 20:53 UTC (SLWC). The 00:00 and 12:00 local times (LT) are
 868 highlighted by 2 vertical dashed lines.

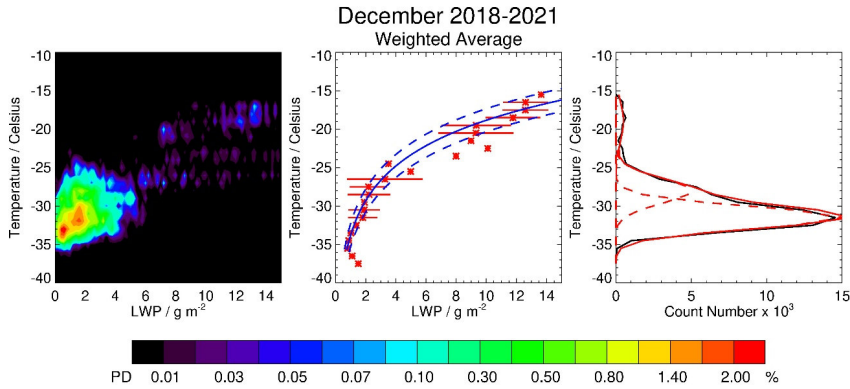
869

870



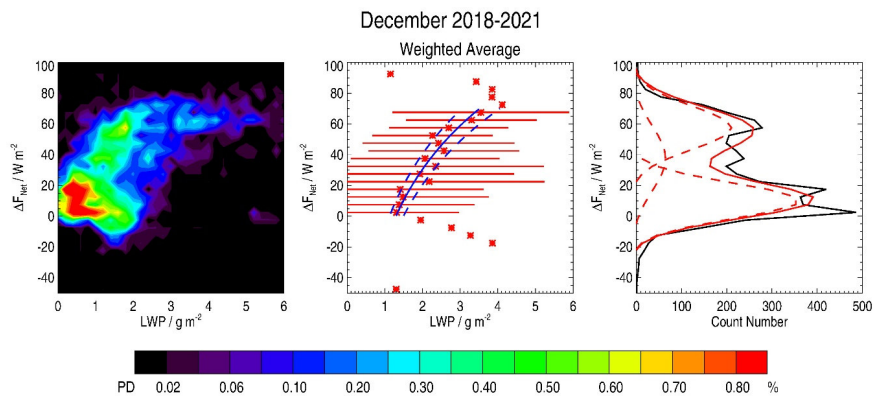
871
 872 **Figure 3:** (from top to bottom) Time evolution (UTC, hour) of the cloud radiative forcing
 873 component (ΔF_{net}) (W m^{-2}) and its individual components: (ΔF) (W m^{-2})—calculated on 27
 874 December 2021: (from top to bottom) net (ΔF_{net}), downward longwave downward (ΔF_{LW}^{Down}),
 875 upward longwave upward (ΔF_{LW}^{Up}), downward shortwave downward (ΔF_{SW}^{Down}) and upward
 876 shortwave upward (ΔF_{SW}^{Up}) calculated on 27 December 2021. The SLW cloud layer (if present)

877 is highlighted by a red area in the uppermost panel, with the height on the y-axis shown on the
878 right. The 00:00 and 12:00 local times (LT) are highlighted by 2 vertical blue dashed lines.
879

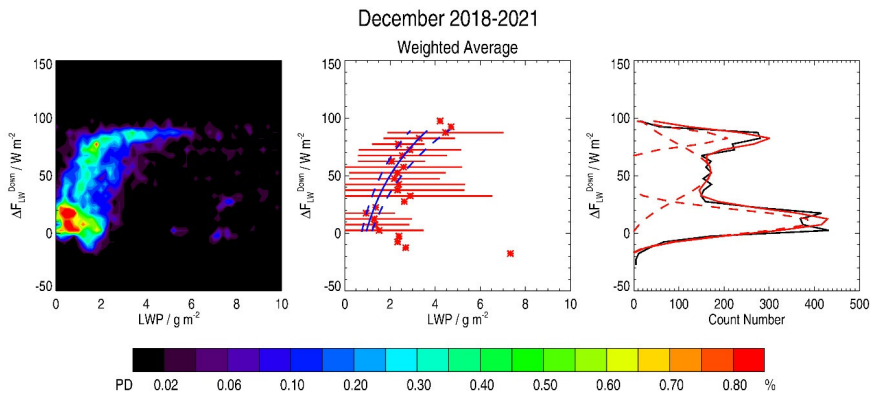


880
881 **Figure 4:** (Left) Probability Density (PD, %) of the temperature (°C) as a function of Liquid
882 Water Path (LWP, g m⁻²) in the SLWCs in December 2018-2021. The Probability Density is
883 defined in the text. (Centre) Weighted-average LWP vs. temperature (red asterisks) with a fitted
884 logarithmic function (blue solid) encompassing the significant points (within the two dashed
885 blue lines). Horizontal bars represent 1-sigma variability in LWP per 1°C-wide bin. (Right)
886 Temperature as a function of count number per 1°C-wide bin (black solid line) fitted with three
887 Gaussian functions (red dashed curves). The sum of the three Gaussian functions is represented
888 by a red solid line.

889
890



891
 892 **Figure 5:** (Left) Probability Density (PD, %) of the **net**-cloud radiative forcing (ΔF_{net} , W m^{-2})
 893 as a function of Liquid Water Path (LWP, g m^{-2}) in the SLWCs in December 2018-2021. The
 894 Probability Density is defined in the text. (Centre) Weighted-average LWP vs. ΔF_{net} with a
 895 fitted logarithmic function (blue solid) encompassing the significant points (within the two
 896 dashed blue lines). Horizontal bars represent 1-sigma variability in LWP per 5 W m^{-2} -wide bin.
 897 (Right) ΔF_{net} as a function of count number per 5 W m^{-2} -wide bin (black solid line) fitted with
 898 three Gaussian functions (red dashed curves). The sum of the three Gaussian functions is
 899 represented by a red solid line.
 900

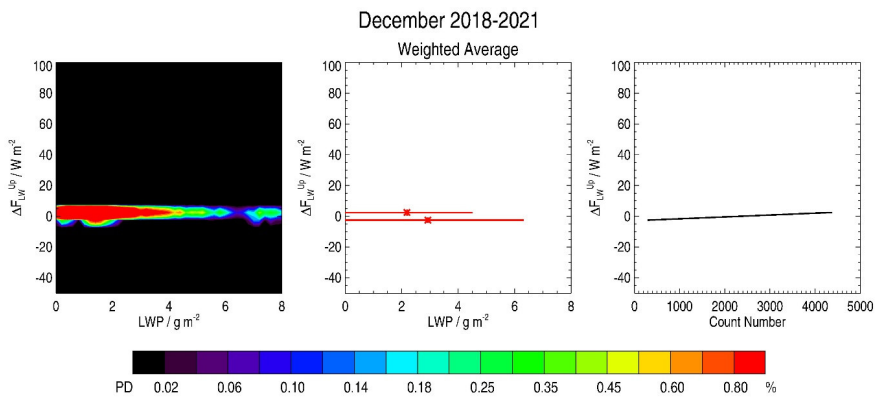


901

902 **Figure 6:** As in Figure 5 but for ΔF_{LW}^{Down} .

903

904



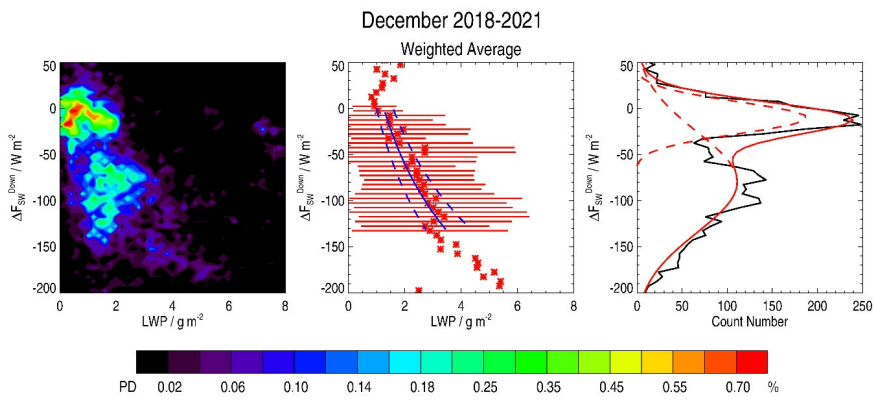
905

906 **Figure 7:** As in Figure 5 but for ΔF_{LW}^{Up} .

907

908

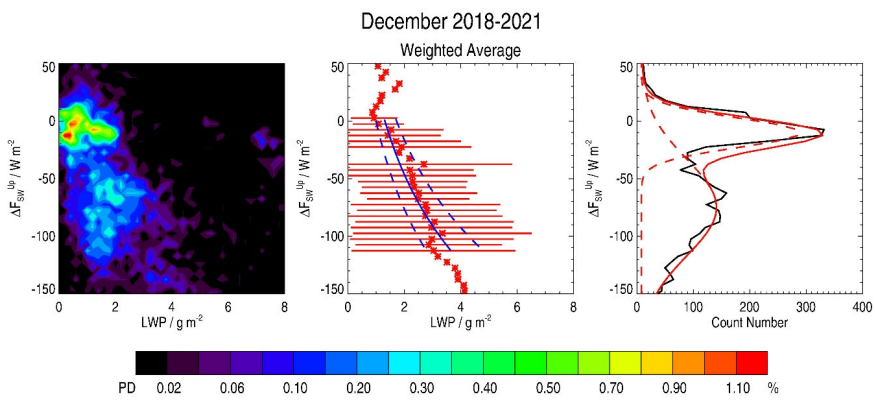
909



910

911 **Figure 8:** As in Figure 5 but for ΔF_{SW}^{Down} .

912



913

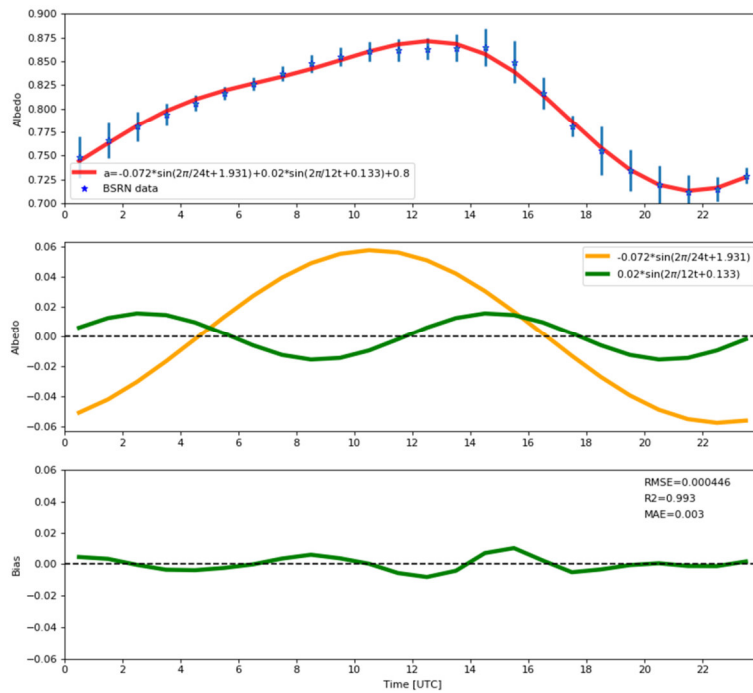
914 **Figure 9:** As in Figure 5 but for ΔF_{SW}^{Up} .

915

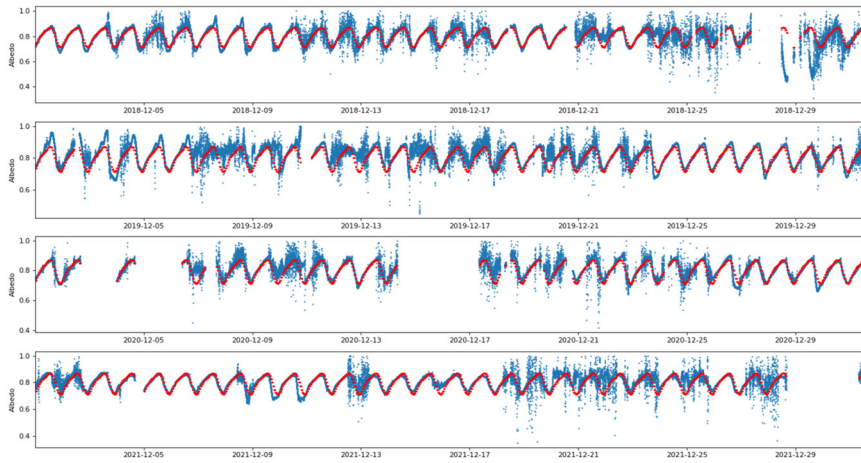


916
917
918
919
920

Figure 10: Image of the sastrugi on the ice surface (Wikimedia Commons).



921
 922 **Figure 4-10:** (Top) Hourly time evolution (UTC, hour) of the mean surface albedo observed
 923 by the BSRN instruments and the associated standard deviation (blue star and vertical bar,
 924 respectively) for the 5 cloud-free periods under consideration in our analysis together with the
 925 fitted trigonometric function based on 2 sine functions (red line). (Centre) The 2 sine functions
 926 fitting the hourly time evolution of the BSRN mean surface albedo. (Bottom) Hourly time
 927 evolution (UTC, hour) of the albedo residuals (BSRN-fit, green line) and corresponding values
 928 of associated Root Mean Square Error (RMSE), Coefficient of determination (R^2), and Mean
 929 Absolute Error (MAE).
 930



931

932 **Figure 1211:** (from top to bottom) Hourly time evolution (UTC) of the surface albedo observed
 933 by the BSRN instruments (blue), and using the fit based on 2 sine functions (red) for the whole
 934 BSRN data set covering the month of December in: 2018, 2019, 2020 and 2021.

935

Page 35 : [1] Tableau mis en forme	RICAUD Philippe	27/11/2023 09:55:00
Tableau mis en forme		
Page 35 : [2] Mis en forme	RICAUD Philippe	27/11/2023 09:56:00
Police :Gras		
Page 35 : [3] Mis en forme	RICAUD Philippe	27/11/2023 09:55:00
Police :Gras		
Page 35 : [4] Mis en forme	RICAUD Philippe	27/11/2023 09:56:00
Police :Gras		
Page 35 : [5] Mis en forme	RICAUD Philippe	27/11/2023 09:55:00
Police :Gras		
Page 35 : [6] Mis en forme	RICAUD Philippe	27/11/2023 09:56:00
Police :Gras		
Page 35 : [7] Mis en forme	RICAUD Philippe	27/11/2023 09:55:00
Police :Gras		
Page 35 : [8] Mis en forme	RICAUD Philippe	27/11/2023 09:56:00
Police :Gras		
Page 35 : [9] Mis en forme	RICAUD Philippe	27/11/2023 09:55:00
Police :Gras		
Page 35 : [10] Mis en forme	RICAUD Philippe	27/11/2023 09:56:00
Police :Gras		
Page 35 : [11] Mis en forme	RICAUD Philippe	27/11/2023 09:55:00
Police :Gras		
Page 35 : [12] Mis en forme	RICAUD Philippe	27/11/2023 09:56:00
Police :Gras		
Page 35 : [13] Mis en forme	RICAUD Philippe	27/11/2023 09:55:00
Police :Gras		
Page 35 : [14] Mis en forme	RICAUD Philippe	27/11/2023 09:56:00
Police :Gras		
Page 35 : [15] Mis en forme	RICAUD Philippe	27/11/2023 09:55:00
Police :Gras		
Page 35 : [16] Mis en forme	RICAUD Philippe	27/11/2023 09:56:00
Police :Gras		
Page 35 : [17] Mis en forme	RICAUD Philippe	27/11/2023 09:55:00
Police :Gras		
Page 35 : [18] Mis en forme	RICAUD Philippe	27/11/2023 09:56:00
Police :Gras		
Page 35 : [19] Mis en forme	RICAUD Philippe	27/11/2023 09:55:00
Police :Gras		
Page 35 : [20] Mis en forme	RICAUD Philippe	27/11/2023 09:56:00
Police :Gras		
Page 35 : [21] Mis en forme	RICAUD Philippe	27/11/2023 09:55:00

Police :Gras

Page 35 : [22] Mis en forme RICAUD Philippe 27/11/2023 09:56:00

Police :Gras

Page 35 : [23] Mis en forme RICAUD Philippe 27/11/2023 09:55:00

Police :Gras

Page 35 : [24] Mis en forme RICAUD Philippe 27/11/2023 09:56:00

Police :Gras

Page 35 : [25] Mis en forme RICAUD Philippe 27/11/2023 09:55:00

Police :Gras

Page 35 : [26] Mis en forme RICAUD Philippe 27/11/2023 09:56:00

Police :Gras

Page 35 : [27] Mis en forme RICAUD Philippe 27/11/2023 09:56:00

Police :Gras

Page 35 : [28] Mis en forme RICAUD Philippe 27/11/2023 09:56:00

Police :Gras

Page 35 : [29] Mis en forme RICAUD Philippe 27/11/2023 09:54:00

Police :Gras

Page 35 : [30] Mis en forme RICAUD Philippe 27/11/2023 09:56:00

Police :Gras

Page 35 : [31] Mis en forme RICAUD Philippe 27/11/2023 09:55:00

Police :Gras

Page 35 : [32] Mis en forme RICAUD Philippe 27/11/2023 09:56:00

Police :Gras

Page 35 : [33] Mis en forme RICAUD Philippe 27/11/2023 09:54:00

Police :Gras

Page 35 : [34] Mis en forme RICAUD Philippe 27/11/2023 09:56:00

Police :Gras

Page 35 : [35] Mis en forme RICAUD Philippe 27/11/2023 09:54:00

Police :Gras

Page 35 : [36] Mis en forme RICAUD Philippe 27/11/2023 09:56:00

Police :Gras

Page 35 : [37] Mis en forme RICAUD Philippe 27/11/2023 09:54:00

Police :Gras

Page 35 : [38] Mis en forme RICAUD Philippe 27/11/2023 09:56:00

Police :Gras

Page 35 : [39] Mis en forme RICAUD Philippe 27/11/2023 09:56:00

Police :Gras

Page 35 : [40] Mis en forme RICAUD Philippe 27/11/2023 09:54:00

Police :Gras

Page 35 : [41] Mis en forme RICAUD Philippe 27/11/2023 09:56:00

Police :Gras

Page 35 : [42] Mis en forme	RICAUD Philippe	27/11/2023 09:54:00
Police :Gras		
Page 35 : [43] Mis en forme	RICAUD Philippe	27/11/2023 09:56:00
Police :Gras		
Page 35 : [44] Mis en forme	RICAUD Philippe	27/11/2023 09:54:00
Police :Gras		
Page 35 : [45] Mis en forme	RICAUD Philippe	27/11/2023 09:56:00
Police :Gras		
Page 35 : [46] Mis en forme	RICAUD Philippe	27/11/2023 09:54:00
Police :Gras		
Page 35 : [47] Mis en forme	RICAUD Philippe	27/11/2023 09:56:00
Police :Gras		
Page 35 : [48] Mis en forme	RICAUD Philippe	27/11/2023 09:54:00
Police :Gras		
Page 35 : [49] Mis en forme	RICAUD Philippe	27/11/2023 09:55:00
Police :Gras		
Page 35 : [50] Mis en forme	RICAUD Philippe	27/11/2023 09:56:00
Police :Gras		
Page 35 : [51] Mis en forme	RICAUD Philippe	27/11/2023 09:54:00
Police :Gras		
Page 35 : [52] Mis en forme	RICAUD Philippe	27/11/2023 09:56:00
Police :Gras		
Page 35 : [53] Mis en forme	RICAUD Philippe	27/11/2023 09:56:00
Police :Gras		
Page 35 : [54] Mis en forme	RICAUD Philippe	27/11/2023 09:55:00
Police :Gras		
Page 35 : [55] Mis en forme	RICAUD Philippe	27/11/2023 09:56:00
Police :Gras		
Page 35 : [56] Mis en forme	RICAUD Philippe	27/11/2023 09:55:00
Police :Gras		
Page 35 : [57] Mis en forme	RICAUD Philippe	27/11/2023 09:56:00
Police :Gras		
Page 35 : [58] Mis en forme	RICAUD Philippe	27/11/2023 09:56:00
Police :Gras		
Page 35 : [59] Mis en forme	RICAUD Philippe	27/11/2023 09:55:00
Police :Gras		